Design of wideband acoustic detectors of gravitational waves equipped with displacement concentrators

Paola Leaci,[1,2,*] Andrea Vinante,[1,3] Michele Bonaldi,[1,3] Paolo Falferi,[1,3] Antonio Pontin,[3] Giovanni A. Prodi,[1,2] and Jean Pierre Zendri[4]

[1]*INFN, Gruppo Collegato di Trento, Sezione di Padova, I-38100 Povo, Trento, Italy*
[2]*Dipartimento di Fisica, Università di Trento, I-38100 Povo, Trento, Italy*
[3]*Istituto di Fotonica e Nanotecnologie, CNR-Fondazione Bruno Kessler, I-38100 Povo, Trento, Italy*
[4]*INFN, Sezione di Padova, Via Marzolo 8, I-35131 Padova, Italy*

(Received 7 November 2007; published 7 March 2008)

We present the concept design of a new class of acoustic detectors of gravitational waves (GWs), which feature a wideband sensitivity. The main novelty relies in the geometry of the test mass, which is equipped with integrated whips. This tapering provides more resonant modes with favorable cross-section to GWs to achieve a large bandwidth. Moreover, the whips act as displacement concentrators and ensure a high mechanical gain at the sensing surfaces. The resulting decrease in mechanical stiffness allows us to achieve the noise matching condition with reasonable operating parameters of the displacement transducer. The performances of the detector are modeled taking into account the quantum and thermal noise sources in the case of a capacitive transducer with a SQUID amplifier. This class of detectors can be designed to target GWs in the frequency range above 1 kHz at a sensitivity comparable to that predicted for future long baseline interferometric detectors. After showing how to scale the design for different constructing materials and target frequencies, we discuss the predicted sensitivity to specific astrophysical signal waveforms.

DOI: 10.1103/PhysRevD.77.062001 PACS numbers: 04.80.Nn, 07.07.Mp, 95.55.Ym

I. INTRODUCTION

The search for gravitational waves (GWs) is being pursued by networks of laser interferometric detectors and resonant detectors. The operating long arm interferometers [1,2] are the GW detectors with the best potential of discovery today, in particular, for GW signals in the lower part of the acoustic frequency band, say $(50 - 2000)$ Hz. In fact, these detectors, which show the best strain sensitivity, are performing coordinated long-term observations and have working plans for near future improvements [3,4].

The operating resonant bar detectors are projects of much smaller size and have been in long-term operation for many years [5,6]. Their sensitivity is limited in a narrow frequency range around 900 Hz. This is a consequence of their conventional detection design, where a lighter mechanical resonator is coupled and tuned to a resonant mode of the larger test mass sensitive to GWs. The lighter resonator provides a mechanical amplification of the deformation of the test mass around its resonance frequency. This amplification is necessary to overcome the additive noise contributed by the electrical signal amplifier and, if possible, to achieve the noise matching condition [7]. Unavoidably, the lighter resonator produces also additional thermal noise, which dominates the performances of the detectors out from its resonance. This conventional scheme of resonant detection can be improved by using a chain of tuned resonators with decreasing masses [8], but the additional thermal noise limits in practice the bandwidth to $\lesssim 0.1$ of the resonance frequency. The state-of-the-art is represented by the AURIGA bar detector, which implements a chain of two lighter resonators tuned to the first longitudinal mode of the cylindrical bar [9]. The current designs of spherical resonant detectors are affected as well by this limitation [10].

New concept designs of acoustic detectors have been proposed to overcome the bandwidth limitations of conventional resonant detectors: the DUAL detectors [11,12] are sensitive over a wide frequency bandwidth between the fundamental quadrupolar resonant modes of the two nested test masses. To preserve the wide frequency band and to minimize the thermal noise, the DUAL detectors need a geometrically selective readout, which senses the quadrupolar deformations, as those produced by GWs, while rejecting deformations with different symmetry [12]. More recently, the same operating principle has been demonstrated also in the case of a hollow cylindrical test mass, called single-mass DUAL detector [13]. It has been proved that the latter can offer all the advantages of a DUAL detector, but with easier detector realization. Both these designs, however, set too strict requirements on the noise stiffness of the motion sensors. In fact, it is well known in linear system theory that the limiting performances can be achieved only if the measuring device has a noise impedance matched to the impedance of its load (see, e.g., Ref. [14]). The noise stiffness required to optimize the performance of the single-mass DUAL proposed in Ref. [13] is 2-3 orders of magnitude larger than the one which could be achieved by realistic readouts, both elec-

*Corresponding author: leaci@science.unitn.it

tromechanical and optomechanical. Therefore, also the DUAL detectors require a wideband mechanical amplification of displacement, which cannot be of the traditional resonant type, as above mentioned.

In this article, we propose a new design of single hollow test mass which allows us to achieve the noise matching condition with realistic displacement transducers. In this design, the test mass is equipped with displacement concentrators made by properly tapered whips [15], which provide wideband mechanical amplification at the sensing surfaces. Moreover, the test mass design is optimized so that five resonant modes with favorable cross-section to GWs contribute to its wideband sensitivity, as compared with the two modes contributing to the sensitivity of the single-mass DUAL detector. As in former DUAL designs, also the new ones exploit the back-action reduction at frequencies between adjacent resonant modes. The resulting main advantage of the new design is the reduction of the mechanical stiffness at the sensing surfaces by almost 3 orders of magnitude. This allows us to achieve the noise matching condition, while keeping a standard quantum limit (SQL) performance comparable to the DUAL detectors, in terms of noise spectra. The development of this new design was based on the systematic use of three-dimensional dynamical simulations by means of finite element method (FEM).

The paper is organized as follows. In Sec. II, we briefly review the model of a generic acoustic detector made by a single test mass equipped with an ideal SQL readout or a realistic capacitive transducer. Section III describes the new concept design, namely, the design of the test mass, the design of the capacitive displacement transducer and amplification chain, and the resulting design sensitivity. Section IV is devoted to the discussion of a few science cases, based on two detector configurations targeted to different frequency bandwidths: $\sim(1.1-2.6)$ kHz and $\sim(2-5)$ kHz. Conclusions are summarized in Sec. V.

II. GENERAL PROPERTIES OF ACOUSTIC GW DETECTORS

The fundamental driving forces on the test mass of an acoustic GW detector are the tidal force field of the GW, the readout back-action force and the thermal noise. In the following subsections we recall the system response on the basis of the guidelines of Refs. [12,13], and we discuss the noise matching condition to a capacitive readout. We also review the general scaling properties of the mechanical design of the cylindrical test mass in terms of its dimensions and related operating frequencies.

A. Response of the test mass to the fundamental driving forces

The deformation $\mathbf{u}(\mathbf{r}, t)$ of the test mass is read at the selected sensing surfaces and the output displacement can be expressed as

$$X(t) = \int_S ds \mathbf{P}(\mathbf{r})\mathbf{u}(\mathbf{r}, t), \tag{1}$$

where $\mathbf{P}(\mathbf{r})$ is a suitable weight function, used to select the deformations that can be produced by the quadrupolar GW field and to reject deformations of different geometrical symmetry.

As usual, in the following $h(t)$ is the time varying amplitude of metric perturbation related to GW. The detector responses to $h(t)$ and to an input back-action force $F_{\mathrm{BA}}(t)$ are described in the frequency domain by

$$\tilde{X}(\omega) = \tilde{h}(\omega)H_{\mathrm{GW}}(\omega) \tag{2}$$

and

$$\tilde{X}(\omega) = \tilde{F}_{\mathrm{BA}}(\omega)T_{\mathrm{BA}}(\omega), \tag{3}$$

where a tilde denotes a Fourier transform. The back-action force acts on the sensing surfaces and it is basically determined by the readout. The function $|T_{\mathrm{BA}}(\omega)|^{-1}$ is the mechanical stiffness $k(\omega)$ of the readout port of the test mass.

The expressions of the transfer functions, in terms of the superposition of the resonant modes of the test mass, are

$$H_{\mathrm{GW}}(\omega) = \frac{1}{2V}\sum_m \frac{-\omega^2[\int_V dV \mathbf{W}(\mathbf{r})\cdot\mathbf{w}_m(\mathbf{r})][\int_S ds \mathbf{P}(\mathbf{r})\cdot\mathbf{w}_m(\mathbf{r})]}{(\omega_m^2-\omega^2)+i\omega_m^2\phi_m(\omega)} \tag{4}$$

and

$$T_{\mathrm{BA}}(\omega) = \frac{1}{M}\sum_m \frac{[\int_S ds \mathbf{P}(\mathbf{r})\cdot\mathbf{w}_m(\mathbf{r})]^2}{(\omega_m^2-\omega^2)+i\omega_m^2\phi_m(\omega)}, \tag{5}$$

where the integrals are performed on the volume V and sensing surfaces S of the test mass. Here $\mathbf{W}(\mathbf{r})$ is the spatial component of the GW field, M is the mass of the detector, ω the angular frequency, $\mathbf{w}_m(\mathbf{r})$ and ω_m the displacement field and the resonance angular frequency of the normal mode m, respectively. For frequency-independent losses, the phase lag $\phi_m(\omega)$ is equal to the inverse of the material quality factor Q [16].

For a system at equilibrium with a bath at temperature T, the fluctuation-dissipation theorem [17] predicts the following single sided power spectrum of the thermal noise on the output variable X,

$$S_{XX}(\omega, T) = \frac{-4K_BT}{\omega}\Im m[T_{\mathrm{BA}}(\omega)], \tag{6}$$

where K_B is the Boltzmann constant.

B. Noise matching and mechanical amplification

The test mass has to be equipped with a readout system. The noise power spectral densities contributed by the readout are $S_{xx}(\omega)$ (m^2/Hz) and $S_{ff}(\omega)$ (N^2/Hz), that represent the additive noise in terms of equivalent displacement

and the back-action force disturbance on the test mass, respectively. Then, the noise on the measured observable X due to the readout can be simply expressed by

$$S_{XX}^{R}(\omega) = S_{xx}(\omega) + |T_{\mathrm{BA}}(\omega)|^2 S_{ff}(\omega). \tag{7}$$

It is convenient to introduce also the energy resolution, expressed as number of energy quanta,

$$\epsilon_R(\omega) = \frac{\sqrt{S_{xx}(\omega)S_{ff}(\omega)}}{\hbar} \tag{8}$$

and the readout noise stiffness:

$$k_R(\omega) = \sqrt{\frac{S_{ff}(\omega)}{S_{xx}(\omega)}}. \tag{9}$$

Then, it is straightforward to show [13] that the minimum readout noise, for given $\epsilon_R(\omega)$ and $T_{\mathrm{BA}}(\omega)$, is achieved when

$$k_R(\omega) = k(\omega), \tag{10}$$

where $k(\omega) = |T_{\mathrm{BA}}(\omega)|^{-1}$. According to Eq. (10), we optimize the coupling between the test mass and its transducer by matching the readout noise stiffness k_R to the mechanical stiffness k of the test mass. For instance, in the case of a capacitive transducer, k_R is of the order of $E_0^2 C$ (for detailed calculations see Appendix A), where C is the capacitance of the transducer and E_0 is the bias electric field. Therefore, the noise stiffness can be tuned in principle by acting on E_0. Unfortunately, the breakdown field sets an upper limit to the maximum achievable E_0, which is of the order of 3×10^8 V/m [18]. An ordinary single-mass DUAL [13] would require a noise stiffness of 1.7×10^{11} N/m: even if a readout with a capacitance as large as 10^{-7} F was built, the needed field would be $\sim 10^9$ V/m, clearly out of reach.

The straightforward way to relax the requirement on the readout noise stiffness is to increase the mechanical deformation on the sensing surfaces. The surface integral in Eqs. (4) and (5),

$$\Gamma_m = \int_S ds \mathbf{P}(\mathbf{r}) \cdot \mathbf{w}_m(\mathbf{r}), \tag{11}$$

can be interpreted as an estimate of the displacement concentration relative to the mth mode over the sensing surface. Close to the resonant frequencies of the test mass, the readout noise stiffness required to achieve the noise matching is reduced by the square of the displacement concentration Γ_m. In fact, near ω_m, the transfer functions $H_{\mathrm{GW}}(\omega)$ and $T_{\mathrm{BA}}(\omega)$ are dominated by the response of the mth mode so that $|H_{\mathrm{GW}}| \propto \Gamma_m$ and $|T_{\mathrm{BA}}| \propto \Gamma_m^2$; therefore, according to Eq. (10), we have $k_R(\omega) \propto 1/\Gamma_m^2$. However, in order to increase the coefficients Γ_m, one needs to change the detector geometry, for instance by adding some kind of embedded mechanical amplification stage.

The best achievable sensitivity is affected by the test mass geometry: whenever this geometry is changed, one needs to check that the sensitivity is preserved. To discuss this point, let us consider the detector noise in terms of GW strain at input,

$$S_{hh}(\omega, T) = S_{hh}^{R}(\omega) + \frac{S_{XX}(\omega, T)}{|H_{\mathrm{GW}}(\omega)|^2}, \tag{12}$$

where

$$S_{hh}^{R}(\omega) = \frac{\hbar \epsilon_R(\omega)}{|H_{\mathrm{GW}}(\omega)|^2}\left[\frac{1}{k_R(\omega)} + |T_{\mathrm{BA}}(\omega)|^2 k_R(\omega)\right] \tag{13}$$

is the detector noise obtained when the thermal noise is neglected. In this approximation, assuming the readout optimally matched ($k_R(\omega) = |T_{\mathrm{BA}}(\omega)|^{-1}$) and with quantum limit energy resolution ($\epsilon_R(\omega) = 1$) [19], Eq. (13) gives the so-called SQL sensitivity of the detector:

$$S_{hh}^{\mathrm{SQL}}(\omega) = 2\hbar \frac{T_{\mathrm{BA}}(\omega)}{|H_{\mathrm{GW}}(\omega)|^2}. \tag{14}$$

According to Eqs. (4) and (5), around ω_m, the SQL sensitivity does not depend on the change of the displacement concentration Γ_m. This happens because the term representing the displacement concentration dominates at resonance both in the numerator and denominator of Eq. (14). However, this is not the case of a wideband detector, which works in-between resonances. Thus one has always to check *a posteriori* if the detector SQL sensitivity is preserved when a mechanical amplification stage is implemented. For instance, it has been demonstrated that the implementation of leverage type amplifiers [20], suitable to solve the noise matching, can strongly degrade the SQL sensitivity of the ordinary single-mass DUAL detector [21].

C. Scaling formulas

The scaling formulas will be used throughout the paper to evaluate the sensitivity of detectors made by different materials and with scaled dimensions. The scaling of the vibrational spectrum of a three-dimensional body, when its size and/or material are changed, can be obtained by studying the Rayleigh quotient $\mathcal{R}$ of the system [22]. The Rayleigh quotient, based on the principle that a conservative system vibrating at a natural frequency has maximum system kinetic energy equal to the maximum system potential energy, is a popular means of estimating frequencies in linear undamped vibratory systems. A detailed treatment shows that $\mathcal{R}$ has stationary points at the system eigenfunctions $\mathbf{w}_m$, and these stationary values are the system eigenvalues $\mathcal{R}(\mathbf{w}_m) = \omega_m^2$ [23].

Let us show now as the Rayleigh quotient is defined on a free harmonic vibration of a three-dimensional elastic body, with displacement modal function $\mathbf{w}(\mathbf{r})$ and natural angular frequency $\hat{\omega}$. The solution is expressed as a space x and time t dependent displacement function $\mathbf{w}(\mathbf{r})e^{i\hat{\omega}t}$, and

the maximum stored potential energy is

$$\mathcal{V} = \frac{1}{2}\int_V \sigma_{ij}\varepsilon_{ij}dV, \tag{15}$$

where the strain tensor ε is defined as

$$\varepsilon_{ij} = \frac{1}{2}\left(\frac{\partial w_i}{\partial x_j} + \frac{\partial w_j}{\partial x_i}\right). \tag{16}$$

If the body is made of a material isotropic and homogeneous, the stress components σ_{ij} are given by Hooke's law:

$$\sigma_{ij} = \lambda\varepsilon_{kk}\delta_{ij} + 2\mu\varepsilon_{ij}, \tag{17}$$

where the Lamè coefficients λ and μ depend on the Poisson's ratio σ_p and on the Young's modulus Y of the material:

$$\lambda = \frac{Y\sigma_p}{(1+\sigma_p)(1-2\sigma_p)} \qquad \mu = \frac{Y}{2(1+\sigma_p)}. \tag{18}$$

The kinetic energy associated with the displacement function $\mathbf{w}(\mathbf{r})e^{i\hat{\omega}t}$ is simply:

$$\hat{\omega}^2\mathcal{T} = \hat{\omega}^2\frac{\rho}{2}\int_V (w_i w_i)dV, \tag{19}$$

where $\mathcal{T}$ is the so-called "kinetic energy functional" and ρ is the mass density. The Rayleigh quotient is defined as $\mathcal{R} = \mathcal{V}/\mathcal{T}$ and, if $\mathbf{w}(\mathbf{r})$ is a normal mode, has a stationary point in $\mathbf{w}(\mathbf{r})$ over the space of the possible solutions. In other words, any function $\mathbf{w}'$ obtained from a small variation of $\mathbf{w}$ will give the same value of $\mathcal{R}$ at the first order. This value is exactly the eigenvalue of the mode $\hat{\omega}^2$:

$$\hat{\omega}^2 = \mathcal{R} = \frac{Y}{\rho}\frac{\int_V [\frac{\sigma_p\varepsilon_{kk}}{(1+\sigma_p)(1-2\sigma_p)}\delta_{ij} + \frac{1}{(1+\sigma_p)}\varepsilon_{ij}]\varepsilon_{ij}dV}{\int_V (w_i w_i)dV}, \tag{20}$$

where Eq. (17) has been used to remove any dependence on the stress σ_{ij}. The volume integrals in Eq. (20) are not modified by the choice of Y and/or ρ, then the eigensolution $\mathbf{w}(\mathbf{r})$ remains a stationary point of the Rayleigh quotient whatever the value of Y and/or ρ. On the contrary, the functional dependence on the Poisson's ratio is more complex and there is no guarantee that the solution $\mathbf{w}(\mathbf{r})$ remains a stationary point if σ_p is changed. Moreover we can see that, as the value of $\mathcal{R}$ simply scales as Y/ρ, the corresponding natural frequency will scale as $\sqrt{Y/\rho}$.

The relation expressed by Eq. (20) is also useful to evaluate the effect of the scaling of the elastic body. The solution $\mathbf{w}^*(\mathbf{r}) = \mathbf{w}(\mathbf{r}/a)$ describes a body uniformly expanded by a factor a. By changing the integration variable in Eq. (20), it can be shown that $\mathbf{w}^*(\mathbf{r})$ is a stationary point of $\mathcal{R}$ with a natural frequency $\hat{\omega}^* = \hat{\omega}/a$.

In the case of a solution with cylindrical symmetry, it is also easy to show that $\mathcal{R}$ is independent of the length of the cylinder. Then, in our cylindrical detectors, the angular frequencies of the modes with cylindrical symmetry scale according to the simple relation

$$\frac{\omega_m^*}{\omega_m} = \frac{v_s^*}{v_s}\frac{1}{a_r}, \tag{21}$$

where ω_m, v_s, and ω_m^*, v_s^* are the original and the scaled values of the angular frequency and of the material's sound velocity, respectively. Here a_r is the radial scaling factor.

On the basis of these relations, it is straightforward to evaluate the scaling law for the transfer functions [Eqs. (4) and (5)], in the hypothesis of constant value of the Poisson's ratio and loss angle independent of the frequency. The transfer functions for the scaled system are given as:

$$H_{\mathrm{GW}}^*(\omega) = a_r H_{\mathrm{GW}}\left(\omega\frac{a_r v_s}{v_s^*}\right) \tag{22}$$

and

$$T_{\mathrm{BA}}^*(\omega) = \frac{Y}{Y^*}\frac{1}{a_L}T_{\mathrm{BA}}\left(\omega\frac{a_r v_s}{v_s^*}\right), \tag{23}$$

where a_L is the scaling factor of the cylinder length L. According to Eq. (14), the power spectrum density at the SQL is

$$S_{hh}^*(\omega) = \frac{Y}{Y^*}\frac{1}{a_L a_r^2}S_{hh}\left(\omega\frac{a_r v_s}{v_s^*}\right), \tag{24}$$

while the scaled optimal value for the readout noise stiffness is

$$k^*(\omega) = \frac{a_L Y^*}{Y}k\left(\omega\frac{a_r v_s}{v_s^*}\right). \tag{25}$$

D. Test mass coupled to a capacitive-SQUID readout

In this section we describe how the sensitivity of an acoustic GW detector is affected by a realistic readout, made by a capacitive transducer followed by a SQUID amplifier. A basic scheme of such kind of readout is shown in Fig. 1. The capacitive transducer must be designed in order to implement a selective readout, defined by a properly chosen weight function $\mathbf{P}(\mathbf{r})$ [13]. The coordinate X of the test mass is assumed to be equal to the average gap of the capacitive transducer over the sensing region. This is true in the case of parallel plates. The basic linear equations which describe the coupling between a mechanical and an electrical system through a capacitive transducer, biased with static electric field E_0, are [24]

$$V(t) = E_0 X(t) \tag{26}$$

and

$$F_{\mathrm{BA}}(t) = E_0 Q(t). \tag{27}$$

Equation (26) represents the voltage induced in the electrical circuit by a mechanical displacement X, while Eq. (27) represents the back-action force acting on the

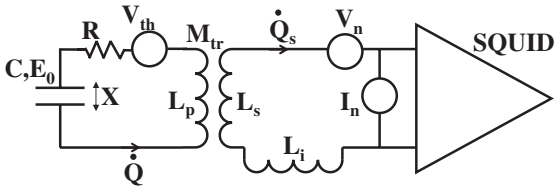

FIG. 1. Electrical scheme of a displacement sensor based on a capacitive transducer and a SQUID amplifier. A displacement X modifies the capacitance C of the transducer, charged with a static field E_0. The induced electrical current is finally measured by the SQUID current amplifier. The intermediate transformer, with primary, secondary, and mutual inductance L_p, L_s, and $M_{\rm tr}$, is required to match the low input inductance L_i of a dc SQUID to the large output impedance of the capacitive transducer. $\dot{Q}$ and $\dot{Q}_s$ are the currents in the primary and secondary coils, and the resistor R represents the total dissipation of the circuit. The electrical noise sources are the additive current noise, I_n, the back-action voltage noise V_n of the SQUID amplifier, and the thermal voltage noise $V_{\rm th}$ related with the dissipation of the electrical circuit.

mechanical system due to a charge Q induced on the capacitor by the electrical circuit (for more details see Appendix A).

Following the method of the normal mode expansion, we write down the equations of motion of the test mass normal modes in the frequency domain, taking into account through Eq. (27) the coupling to the electrical circuit:

$$M[-\omega^2+\omega_m^2+i\omega_m^2\phi_m(\omega)]\tilde{q}_m(\omega) = -\tfrac{1}{2}\rho\omega^2\Lambda_m\tilde{h}(\omega)+\Gamma_m E_0\tilde{Q}(\omega)+\tilde{F}_{{\rm th}-m}(\omega). \quad (28)$$

Here, q_m represents the amplitude of the mth normal coordinate. In the right-hand side of Eq. (28) there are 3 driving terms. The first one is the GW effect, with the coefficients Λ_m defined by

$$\Lambda_m = \int_V dV\mathbf{W}(\mathbf{r})\cdot\mathbf{w}_m(\mathbf{r}). \quad (29)$$

The second one is the back-action term, proportional to $E_0\tilde{Q}(\omega)$ and to the coupling coefficient Γ_m between the mth mode and the readout, i.e., the displacement concentration [see Eq. (11)]. We note that Γ_m and Λ_m depend only on the geometry of the test mass and on the choice of the sensing surface, but not on the electrical circuit parameters. The third driving term is the thermal noise force $F_{{\rm th}-m}$ acting on the coordinate q_m. Its power spectral density is predicted by the fluctuation-dissipation theorem to be

$$S_{F_{{\rm th}-m}}(\omega) = 4k_BTM\omega_m^2\frac{\phi_m(\omega)}{\omega}. \quad (30)$$

Let us discuss the electrical part of the system. The forward (mechanical to electrical) coupling, expressed by Eq. (26), can be rewritten in terms of the normal coordinates q_m as

$$V(t) = E_0\sum_m\Gamma_m q_m(t). \quad (31)$$

In general, if the electrical circuit is read by a SQUID current amplifier, it is convenient to exploit the LC resonance formed by the transducer capacitor C and the inductive part of the circuit. In particular, in order to maximize the noise stiffness of the readout, it is necessary to move the LC resonance frequency close to the design sensitivity band [9]. Because of the small value of the typical input inductance L_i of practical dc SQUIDs, the tuning can be achieved only by interposing a low-loss superconducting matching transformer, as shown in Fig. 1. The effective inductance of the circuit is given by $L_r = L_p - M_{\rm tr}^2/L_t$, where $L_t = L_s + L_i$ and the inductances L_p, L_s, $M_{\rm tr}$, and L_i are shown in Fig. 1. The effective electrical resonance frequency is given by $\nu_{\rm el} = \omega_{\rm el}/(2\pi) = (2\pi\sqrt{L_rC})^{-1}$, and the electrical quality factor is $Q_{\rm el} = \omega_{\rm el}L_r/R$. The equations of motion of the electrical circuit with the intermediate transformer can be written, in the frequency domain, as

$$\begin{cases}(-\omega^2L_p+i\omega R+\frac{1}{C})\tilde{Q}-\omega^2M_{\rm tr}\tilde{Q}_s = E_0\sum_m\Gamma_m\tilde{q}_m+\tilde{V}_{\rm th}\\ -\omega^2M_{\rm tr}\tilde{Q}-\omega^2L_t\tilde{Q}_s = \tilde{V}_n\\ \tilde{I} = \tilde{I}_n+i\omega\tilde{Q}_s.\end{cases} \quad (32)$$

The independent variables are the AC charge on the capacitor Q, the charge on the secondary circuit Q_s and the total current I measured by the amplifier, which is the sum of the physical current $I_s = \dot{Q}_s$ and the additive equivalent noise current I_n, with spectral density S_{I_n}. In addition to the mechanical signal and noise, coupled to the electrical circuit through E_0, we have two electrical noise driving terms: the voltage thermal noise of the electrical circuit $V_{\rm th}$, with power spectral density $S_{V_{\rm th}} = 4k_BTR$ and the voltage back-action noise of the SQUID amplifier V_n, with spectral density S_{V_n}.

Equations (28) and (32) constitute a set of linear stochastic differential equations, which can be solved to yield the total measured SQUID input current I, as function of the different signal and noise driving terms. To obtain the sensitivity of the system as detector of GWs, one has to divide the total measured current noise by the transfer function $I_{\rm GW}(\omega) = \tilde{I}(\omega)/\tilde{h}(\omega)$, which converts an input GW of amplitude $\tilde{h}(\omega)$ to a SQUID input current $\tilde{I}(\omega)$. Equations (28) and (32) constitute an extremely large set of equations, that can be numerically solved only on a finite subset of normal modes. An approximate solution at low frequency can be obtained by considering the first N modes, with N properly chosen in order to achieve a satisfying convergence. Thanks to the selective readout, the transfer functions are well reproduced by taking into account only the normal modes up to the maximum fre-

quency of interest, plus a few higher order modes among those geometrically selected by the readout.

III. DETECTOR DESIGN

The test mass of an acoustic detector can be suitably shaped to achieve the noise matching condition with a practical readout. In this section we propose a new design of a cylindrical detector in which the noise matching condition is achieved by means of displacement concentrators integrated in the test mass. We show that the resulting sensitivity is comparable to that of an ordinary single-mass DUAL detector. Moreover, the SQL sensitivity of the new design can be closely approached by using practical readout configurations. We demonstrate this by using a capacitive-SQUID readout, evolution of those currently under development for resonant detectors [25].

A. Displacement concentrators and selective readout

The test mass design we propose is a substantial progress over the single-mass DUAL detector [13] in two fundamental aspects. In particular, wideband mechanical amplifiers are integrated in the test mass and the dynamics is optimized in order to exploit more modes with favorable cross-section to GWs.

In order to achieve the noise matching, the needed mechanical amplification of the deformation at the sensing surface is about a factor 15–30 with respect to the configuration proposed in Ref. [13]. In a conventional resonant detector this is usually done by means of a resonant transducer with mass much smaller than the one of the test mass [7,26]. This approach however cannot ensure the wideband amplification needed here. An alternative solution to achieve wideband mechanical amplification was proposed long time ago [15], and consists in using tapered elements, the so-called whips. In a whip, the section is progressively (linearly in the simplest version) decreased moving towards its end [see Fig. 2(a)]. A whip behaves as a transverse displacement concentrator. The large base of thickness h_1 is attached to the test body, whose motion is to be amplified, while the other end, of smaller thickness h_2, is left free to move.

The numerical solution of a simple model of the system, based on the Euler-Bernoulli equation [15], shows that such an element provides a conventional resonant amplification in correspondence of the whip transverse standing waves, plus a wideband amplification exclusively due to the geometrical tapering [see Fig. 2(b)]. The latter effect is a consequence of the decrease of the linear mass density moving towards the whip end. In particular, the minimum gain between two consecutive resonances is proportional to the whip-ratio $(h_1/h_2)^{3/4}$. Therefore, a suitable use of a whip element can provide a wideband mechanical amplification between two consecutive whip modes.

As the whips can easily provide a transverse amplification with respect to their base, we developed test mass

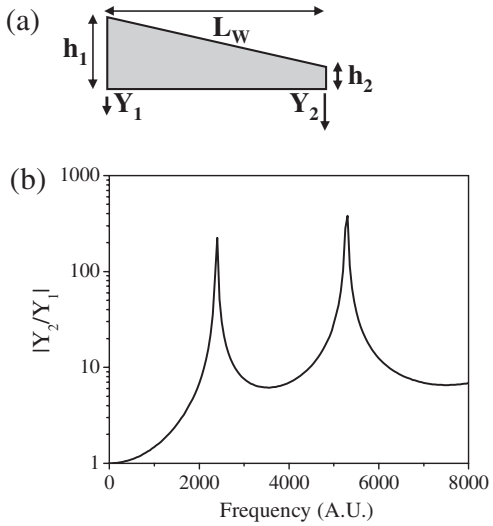

FIG. 2. (a) Simple whip element with linear profile and basic operation principle as mechanical amplification stage. If the base, of thickness h_1, is moved transversely by Y_1, the free end, of smaller thickness h_2, will move by Y_2. (b) The mechanical gain $|Y_2/Y_1|$, as function of the frequency, exhibits conventional resonances, corresponding to the standing transverse waves, plus a wideband gain between two consecutive resonances. The resonance frequencies scale as the ratio h_1/L_W^2, while the minimum value of the off-resonance gain is roughly given by $(h_1/h_2)^{3/4}$ [15].

configurations with external tangential sensing, instead of the internal radial sensing required by the ordinary single-mass DUAL [13]. Two representative configurations are shown in Figs. 3(b) and 3(c). Four main grooves are carried out in the external surface to allow tangential motion in correspondence of the four sensing regions. The profile of the test mass in correspondence of the four main grooves is then tapered to form four pairs of faced whips, which provide mechanical amplification of the cylinder tangential motion. The 8 additional secondary grooves have the only purpose of tuning the frequency of the quadrupolar modes of interest. The whips are designed in order to place the frequencies of the quadrupolar modes of interest of the main body between the frequencies of the first and second mode of the whips. The resulting overall mechanical amplification, with respect to the internal radial deformation, is of about 15 and 30 for the configurations in Figs. 3(b) and 3(c), respectively.

The readout senses the differential motion of the ends of the four pairs of whips (see Fig. 4). The signals from the 4 sensing gaps are combined with quadrupolar symmetry to maximize the response to GW sensitive modes and to reject the effect of other modes. To achieve this condition, the readout has to measure the combination $X(t) = d_{1,2} + d_{3,4} - d_{5,6} - d_{7,8}$, where $d_{i,j}$ is the distance between the ith and jth surfaces (shown by the black segments on the tip of each whip in Fig. 4). As a comparison, Fig. 4 shows also

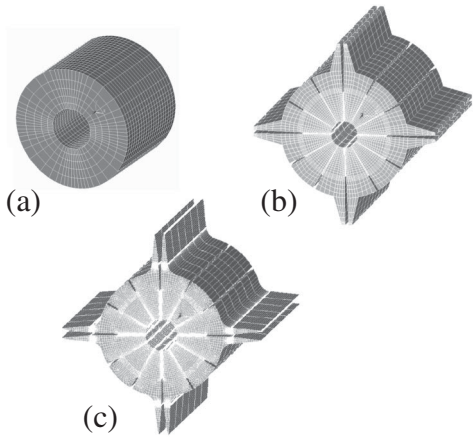

FIG. 3. Different configurations of a hollow cylindrical detector: (a) ordinary single-mass DUAL [13] which is sensitive between the first two quadrupolar modes of the hollow cylinder; (b) cylinder with grooves and whips ensuring a mechanical gain of 15 with respect to the configuration in the panel (a). Its sensitivity bandwidth is determined by the first two quadrupolar modes and the first two whip transverse modes, but its resulting bandwidth is narrower than that of a single-mass DUAL; (c) cylinder with grooves and whips ensuring a mechanical gain of 30 with respect to the configuration in the panel (a). It exploits one additional mode with good cross-section to GW with respect to the configuration in the panel (b) and its resulting bandwidth is as wide as that of a single-mass DUAL. The drawings are not in scale and the geometrical parameters used for the simulations in Sec. III are reported in Table I.

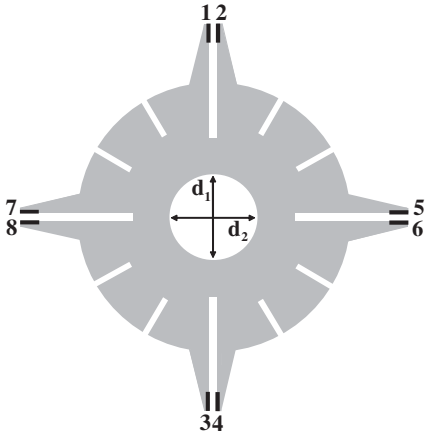

FIG. 4. Measurement readouts that geometrically select the quadrupolar modes of the cylindrical detector. The internal readout ($d_1 - d_2$) was proposed for the single-mass DUAL configuration [see Fig. 3(a)]. The external readout, exploiting the displacement amplification provided by the whips, is used for the tapered configurations in Figs. 3(b) and 3(c). The sensing surfaces are indicated by the black segments on the tip of each whip (1-8). The readout measures $X(t) = d_{1,2} + d_{3,4} - d_{5,6} - d_{7,8}$, where $d_{i,j}$ is the distance between the ith and jth tips.

the sensing areas on the inner hole originally proposed in Ref. [13] for the ordinary single-mass DUAL.

The resulting weight function $\mathbf{P}(\mathbf{r})$ is normal to the reading surface. We chose to normalize $\mathbf{P}(\mathbf{r})$ on a single reading surface S. Therefore, the weight function has the value $+1/S$ for the surfaces 1, 2, 3, 4, and $-1/S$ for the surfaces 5, 6, 7, 8. Outside this domain it goes to zero, since the border effects can be neglected [27].

By simulating gravitational signals propagating along the symmetry axis of the cylinders shown in Fig. 3, we evaluated their responses and calculated the strain noise power spectral densities, following the guidelines of Sec. II. In particular, in order to simulate the transfer function $H_{\mathrm{GW}}(\omega)$, the GW equivalent force, corresponding to an optimal polarization, was applied on the volume of body. The transfer function $T_{\mathrm{BA}}(\omega)$ was evaluated by applying an external force on the readout surfaces. All the simulations were performed by a three-dimensional FEM harmonic analysis by using the ANSYS code [28]. The FEM solver evaluates the transfer functions from the displacement averaged over the readout surfaces according to the weight function used for our measurement strategy and detection scheme. Here we assume, for simplicity, a readout with frequency independent noise properties: ϵ_0, the noise energy, and k_0, the readout noise stiffness that must be properly matched to the detector mechanical stiffness. This is achieved selecting, by visual inspection, the k_0 which makes the flattest sensitivity within the entire bandwidth.

The assumption of a constant noise stiffness is a good approximation of wideband real world transducers. The resulting spectral sensitivity depends on the k_0 value and it occurs that a different choice of k_0 can improve the sensitivity at some frequencies at the cost of a deterioration at other frequencies. Actually, the true SQL spectral sensitivity would be achieved by using a quantum limited readout with a frequency dependent noise stiffness described by Eq. (10), i.e., optimized to the back-action transfer function at each frequency.

In Table I we report the cylinder geometrical parameters and the used material. We will explain our choices of L in Appendix B, where different cylinder lengths are compared.

TABLE I. Geometrical parameters used for the FEM simulations of the molybdenum (Mo) cylinders in Fig. 3. We indicate the cylinder outer and inner radii, its length and mass with r_{ext}, r_{int}, L and M, respectively; r_{ext} does not include the displacement concentrators. The resulting noise stiffness required to match the readout (k_0) is also reported. The material quality factor is assumed $Q = 10^7$ [29].

	r_{ext} (m)	r_{int} (m)	L (m)	M (ton)	k_0 (N/m)
panel (a)	0.5	0.15	3	22	1.7×10^{11}
panel (b)	0.5	0.08	1.7	13.4	5.0×10^{8}
panel (c)	0.35	0.091	1.19	4.4	5.6×10^{7}

B. Design of tapered cylindrical test masses

The configurations proposed in Fig. 3 are optimized for different target frequency bandwidths. In particular, the cylinder in Fig. 3(b) works in the $(2 - 2.7)$ kHz frequency band, while the detectors in Fig. 3(a) and 3(c) are sensitive in the $(2 - 5)$ kHz wider frequency band, as shown in Fig. 5. Such three detectors have large differences in their masses. In fact, the tapered cylinders are much shorter than the ordinary single-mass DUAL to keep the sensitivity bandwidth clean from spurious three-dimensional modes (see Appendix B). However, the SQL sensitivities become comparable if one considers a set of detectors with the same total mass. For instance, the resulting SQL performance of 5 independent tapered detectors of type Fig. 3(c) is approximately equivalent to the single-mass DUAL configuration.

The configuration in Fig. 3(c) represents an optimal design for a wideband sensitivity. It differs from the configuration in Fig. 3(b) for the different shape of the whips, that produces a wider spacing of the sensitive modes and a lower mechanical stiffness. This leads to wider bandwidth and lower optimal noise stiffness of the readout. In fact, k_0 at the sensing surfaces is reduced by $\sim$3 orders of magnitude.

Moreover, five resonant modes with favorable cross-section to GWs contribute to the wideband sensitivity of the tapered cylinder in Fig. 3(c), as compared with the two modes contributing to the sensitivity of the ordinary single-mass DUAL detector [13]. This feature is shown in Fig. 27(a).

If the thermal noise contribution is taken into account for the configurations of Figs. 3(b) and 3(c), we obtain the sensitivity curves plotted in Figs. 6 and 7, respectively. A useful benchmark to compare the performances of these detectors is the sensitivity to short GW pulses, $\tilde{H} = [\frac{2}{\pi} \times \int_0^{+\infty} \frac{1}{S_{hh}(\omega)} d\omega]^{-1/2}$. $\tilde{H}$ is obtained by setting the signal-to-noise ratio (SNR) [see Eq. (37)] equal to one. According to Tables II and III, the cooling of the detector at 100 mK or below is required to approach the SQL sensitivity within a factor $\gtrsim 2$, if the value $Q = 10^7$ is used.

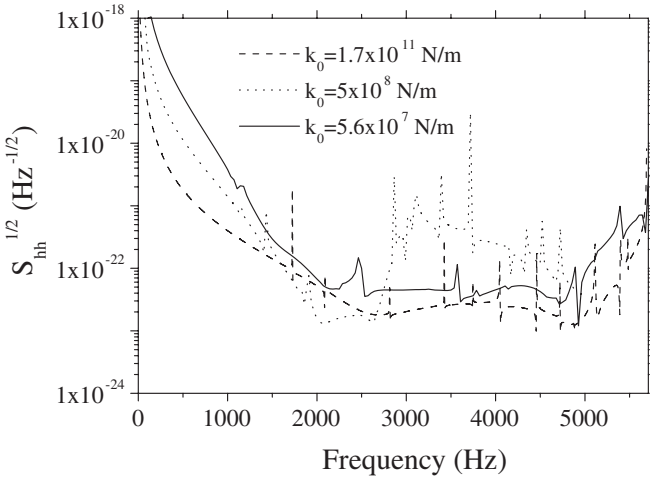

FIG. 5. SQL sensitivities for the cylinders in Fig. 3(a) (dashed curve), Fig. 3(b) (dotted curve), and Fig. 3(c) (solid curve). The configuration in Fig. 3(c) shows the lowest stiffness.

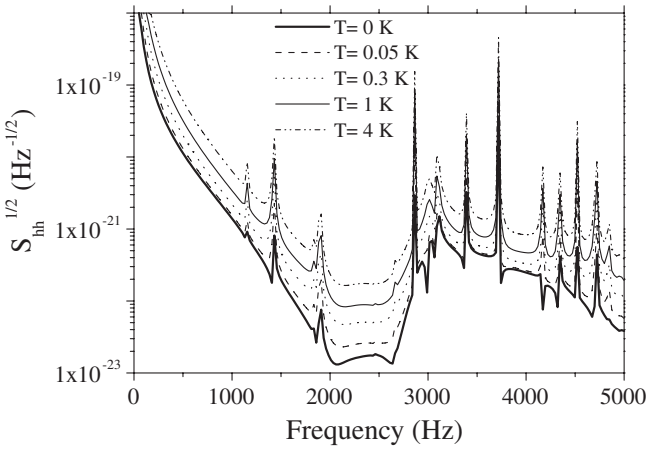

FIG. 6. Total power spectral densities for the cylinder in Fig. 3(b), evaluated at a number of temperatures. The corresponding sensitivities to short pulses, $\tilde{H}$, are reported in Table II. A constant value $Q = 10^7$ is used in the simulations. The noise stiffness of the configuration is $k_0 = 5 \times 10^8$ N/m.

C. Coupling of the tapered test masses to a capacitive-SQUID readout

In this section we consider the tapered test masses proposed in Sec. III B coupled to a capacitive-SQUID readout. A first relevant issue is to find a way to realize a selective readout of the quadrupolar modes, which imple-

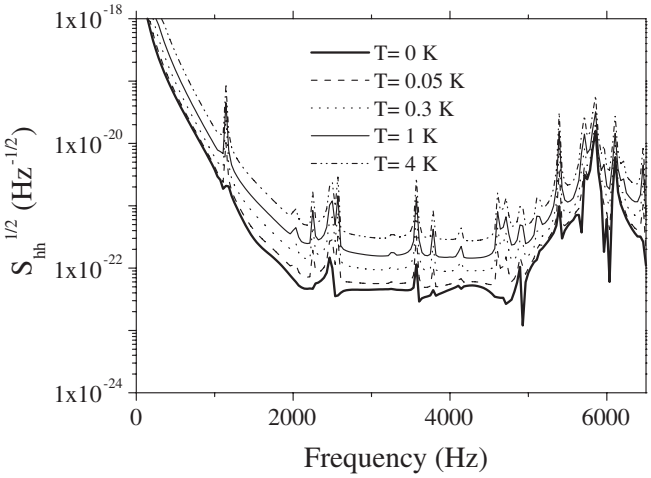

FIG. 7. Total power spectral densities for the configuration of Fig. 3(c), evaluated at a number of temperatures. The corresponding sensitivities $\tilde{H}$ are reported in Table III. A constant value $Q = 10^7$ is used in the simulations. The noise stiffness of the configuration is $k_0 = 5.6 \times 10^7$ N/m.

TABLE II. Pulse amplitude $\tilde{H}$ detected with unitary SNR for the sensitivity curves plotted in Fig. 6.

Temperature (K)	$\tilde{H}$ (Hz^{-1})
0	2.7×10^{-25}
0.05	4.5×10^{-25}
0.3	9.1×10^{-25}
1	1.6×10^{-24}
4	3.1×10^{-24}

TABLE III. Pulse amplitude $\tilde{H}$ obtained with unitary SNR for the sensitivity curves shown in Fig. 7.

Temperature (K)	$\tilde{H}$ (Hz^{-1})
0	3.6×10^{-25}
0.05	5.7×10^{-25}
0.3	1.0×10^{-24}
1	1.7×10^{-24}
4	3.3×10^{-24}

ments the weight function $\mathbf{P}(\mathbf{r})$ introduced in Sec. III A. A possible solution is shown in Fig. 8, and consists in a series connection of four identical capacitors, each one of capacitance $4C$. The capacitor plates are placed at the end of two faced whips, and the variable gap of each capacitor is constituted by the distance between the plates. The capacitors must be alternately charged with a static bias field $+E_0$ or $-E_0$, where the sign corresponds to the voltage drop across the capacitor measured in the direction of the arrow in Fig. 8. In principle, this can be achieved without any additional component, because each capacitor acts as a decoupling capacitor for the following or preceding capacitor.

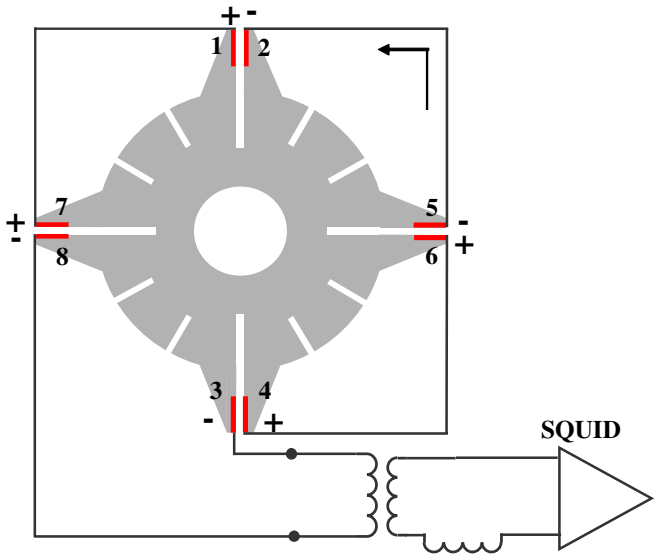

FIG. 8 (color online). Possible reading scheme of the tapered cylinder by means of a capacitive transducer. There are 4 sensing regions, each one in correspondence to the end of a pair of whips. A capacitor is formed in each sensing region, and the 4 capacitors are connected in series. Assuming equal average gaps, the same static bias field E_0 can be stored in each capacitor, with alternate sign. This scheme allows a selective readout of the quadrupolar modes of the test mass implementing the optimal weight function $\mathbf{P}(\mathbf{r})$.

The AC voltage signal across the series of the four capacitors is given, at first order in the capacitor averaged gap variation $d_{i,j}$, by

$$V(t) = E_0(d_{1,2} + d_{3,4}) - E_0(d_{5,6} + d_{7,8}) = E_0 X(t). \quad (33)$$

At the same time, if an AC charge $Q(t)$ is induced by the electrical circuit on the series-connected capacitors, the same charge Q will appear on each single capacitor. This generates a force $F = \pm E_0 Q$ onto the plates of the capacitor, where the sign + holds for the capacitor 1, 2, 3, 4, and the sign − for the capacitor 5, 6, 7, 8. More precisely, the back-action force acting on the test mass can be written in the following compact form:

$$\mathbf{F}_{\mathbf{BA}}(\mathbf{r}, t) = E_0 Q(t) \mathbf{P}(\mathbf{r}). \quad (34)$$

Therefore we can identify $E_0 Q(t)$ as the scalar back-action force $F_{\mathrm{BA}}(t)$ [see Eq. (27)].

Now we can make explicit calculations of the sensitivity of the test mass–readout system for some test mass configurations by using the method described in Sec. II D. We use a set of fixed parameters, listed in Table IV. Moreover, for a given test mass, we modify two parameters, the electrical bias field E_0 and the electrical circuit resonance frequency ν_{el}, which fixes the value of the primary inductance L_p. This allows us to make a rough sensitivity optimization; ν_{el} is placed roughly at the midpoint of the sensitivity band. However, the sensitivity curve depends quite weakly on ν_{el}, at least for variations up to 20%. E_0 is set to the lowest value required to make the final sensitivity curve reasonably flat. The corresponding approximated noise stiffness $E_0^2 C$ (see Appendix A) is roughly half the optimum noise stiffness obtained by using the generic ideal readout.

TABLE IV. Common parameters used for the electromechanical numerical simulations. See Fig. 1 for the description of electrical components.

Parameter	Value
T	50 mK
ϕ_m	10^{-7}
C	5×10^{-9} F
Q_{el}	2×10^6
L_s	5.1×10^{-6} H
$M_{\mathrm{tr}}/\sqrt{L_p L_s}$	0.9
L_i	1.6×10^{-6} H
$\epsilon_{I_n} \equiv L_i S_{I_n}/2$	$1\ \hbar$
$\epsilon_{V_n} \equiv S_{V_n}/(2\omega^2 L_i)$	$1\ \hbar$

The sensitivities of the test masses described in Figs. 3(b) and 3(c), equipped with a capacitive-SQUID readout, are comparable with the analogous configurations equipped with a quantum limit readout (see Figs. 9 and 10, respectively). In particular, even though the resulting noise spectrum is not so much flat over the bandwidth, the sensitivity to short GW bursts is only about $\sqrt{2}$ higher.

As shown in Figs. 9 and 10, it occurs that at some frequencies the noise spectrum of a tapered cylinder equipped with a capacitive-SQUID readout is lower than the quoted SQL noise. This is not a paradox because the quoted SQL refers to a quantum limited readout with the constraint of a constant noise stiffness k_0, which makes it worse than the true quantum limit. Therefore, a readout with a different noise stiffness might perform better at some frequencies and worse at others.

The most critical parameters are the energy sensitivity of the SQUID amplifier $(\epsilon_{I_n}, \epsilon_{V_n})$ at 1 $\hbar$, close to the quantum limit value, the electrical quality factor $Q_{\rm el} = 2 \times 10^6$ and the bias field $E_0 \sim 1 \times 10^8$ V/m. The last two values are close to those achieved by state-of-the-art technology, while a factor 10 improvement is required on the energy sensitivity of the SQUID amplifier demonstrated in a strongly coupled configuration. However, no one of these goals is out of reach within current R&D programs. Greater values of E_0 produce flatter sensitivity curves, but they are not potentially achievable. The thermal noise is computed assuming $T/Q = 5 \times 10^{-9}$ K (which can be achieved with a low-loss material at $T < 1$ K), an effective electrical frequency $\nu_{\rm el} = 2420$ Hz in Fig. 9, and equal to 3630 Hz in Fig. 10.

For comparison, we show in Fig. 11 the sensitivities of the ordinary single-mass DUAL depicted in Fig. 3(a), equipped with a quantum limit readout and with a capacitive-SQUID readout. For the latter case we consider both a realistic readout configuration as in Fig. 10 and an unrealistic one with a bias field $E_0 \sim 3 \times 10^9$ V/m. A comparison of Figs. 9 and 10 with Fig. 11 clearly shows the most relevant advantage of the new tapered concept design with displacement concentrators: the requirements on the readout parameters are much more relaxed, so that the SQL sensitivity can be approached with the state-of-the-art transducers.

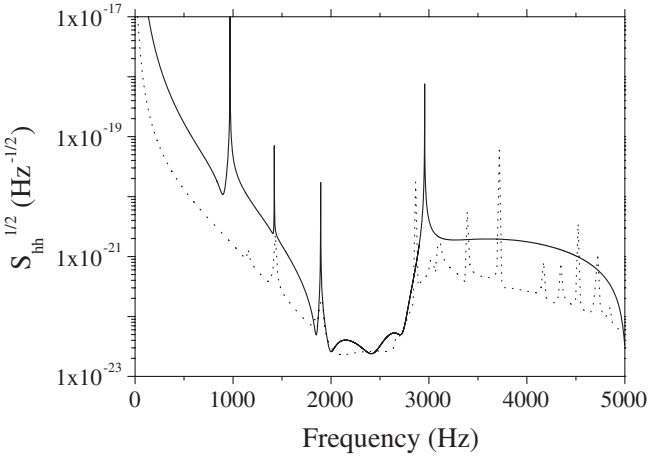

FIG. 9. Sensitivities for the cylinder in Fig. 3(b). Solid curve: the cylinder is equipped with a capacitive-SQUID readout, $E_0 \sim 1.4 \times 10^8$ V/m, $\nu_{\rm el} = 2420$ Hz and the other parameters as in Table IV; $\tilde{H} = 6 \times 10^{-25}$ Hz^{-1}. Dotted curve: the cylinder is equipped with a quantum limited readout, $k_0 = 5 \times 10^8$ N/m; $\tilde{H} = 4.5 \times 10^{-25}$ Hz^{-1}.

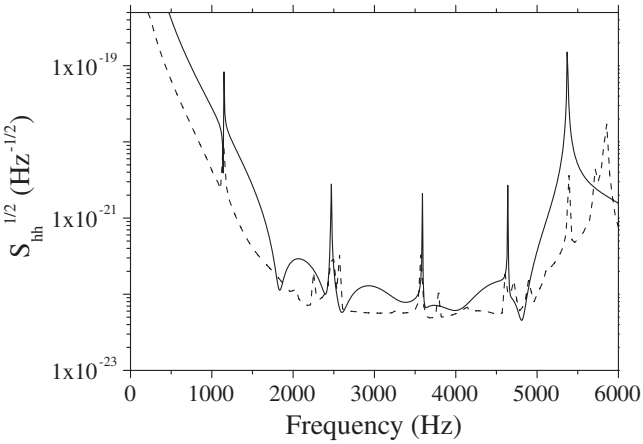

FIG. 10. Sensitivities for the detector in Fig. 3(c). Solid curve: the detector is equipped with a capacitive-SQUID readout, $E_0 \sim 6.5 \times 10^7$ V/m, $\nu_{\rm el} = 3630$ Hz and the other parameters as in Table IV; $\tilde{H} = 8.2 \times 10^{-25}$ Hz^{-1}. Dotted curve: the detector is equipped with a quantum limited readout, $k_0 = 5.6 \times 10^7$ N/m; $\tilde{H} = 5.7 \times 10^{-25}$ Hz^{-1}.

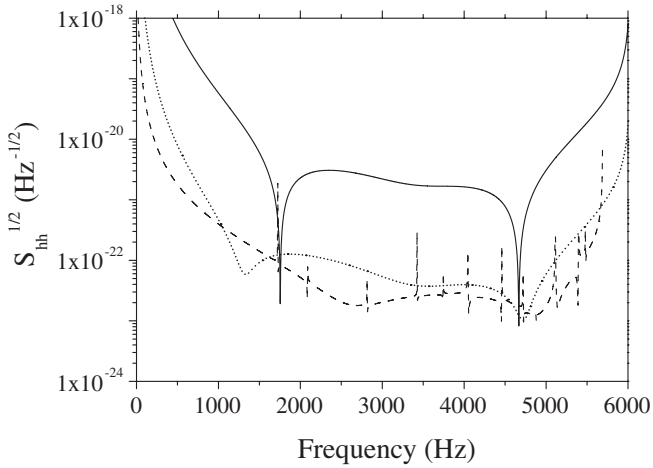

FIG. 11. Sensitivities for the ordinary single-mass DUAL [Fig. 3(a)]. Solid curve: capacitive-SQUID with same realistic parameters as in Fig. 10; $\tilde{H} = 1.7 \times 10^{-24}$ Hz^{-1}. Dotted curve: capacitive-SQUID with same parameters, but with an unrealistic electrical field $\sim 3 \times 10^9$ V/m; $\tilde{H} = 2.8 \times 10^{-25}$ Hz^{-1}. Dashed curve: quantum limited readout, $k_0 = 1.7 \times 10^{11}$ N/m; $\tilde{H} = 1.3 \times 10^{-25}$ Hz^{-1}.

IV. SELECTED SCIENCE CASES

In the following we discuss a few different detector configurations, targeted to different science cases. The directional response of tapered cylinders to GWs results identical to that of an interferometric detector with two 90° arms. We focus on the optimal design of tapered detectors for two different frequency bandwidths and estimate the SNR for GW sources as merging binary neutron stars (NSs) and black holes (BHs).

A. Directional response

We computed the transfer function $H_{\mathrm{GW}}(\omega)$ of the tapered detector by three-dimensional FEM evaluations, assuming that a plane gravitational wave is arriving from the direction (θ, φ) with an arbitrary polarization ψ. The dependence of $H_{\mathrm{GW}}(\omega)$ from the wave direction and polarization is usually described by the *antenna pattern*. This is a function of θ, φ, ψ, computed for each frequency as

$$F(\theta, \varphi, \psi) = \frac{|H_{\mathrm{GW}}(\omega)|}{\max\{|H_{\mathrm{GW}}(\omega)|\}}, \tag{35}$$

where $\max\{|H_{\mathrm{GW}}(\omega)|\}$ indicates the maximum value of the modulus of $H_{\mathrm{GW}}(\omega)$ over θ, φ, ψ.

The detector antenna patterns to the two independent polarization components of the GW (plus $\psi = 0$ and cross $\psi = \pi/4$) are shown in Figs. 12 and 13, respectively. Both responses are equal to those of an interferometric GW detector, with arms oriented along the X and Y axes.

The angles θ and φ are the usual spherical-polar coordinates, representing the wave travelling direction, as measured in the detector reference frame, where θ is the angle with the axis of the cylinder and $\varphi = 0$ is a semiplane cutting between two faced whips. Figures 12 and 13 show the antenna pattern also in terms of Cartesian coordinates,

$$\begin{cases} X = F\sin(\theta)\cos(\varphi) \\ Y = F\sin(\theta)\sin(\varphi) \\ Z = F\cos(\theta), \end{cases} \tag{36}$$

where the symbol F represents the modulus of $F(\theta, \varphi, \psi)$. In particular, it is indicated as $|F_+^+|$ and $|F_+^\times|$ for the plus polarization component (see Fig. 12) and for the cross polarization component (see Fig. 13), respectively. Similarly, a tapered cylinder, rotated by 45° in the XY plane with respect to the first detector, will exhibit analogous response functions, $F_\times^+$ and $F_\times^\times$, but rotated along φ by $\pi/4$.

To improve the antenna pattern characteristics, it is convenient to consider a composite detector made by two colocated tapered detectors with parallel cylindrical axes and rotated in the XY plane by $\pi/4$ with respect to each other. This composite detector would need a housing larger by just a few cubic meters. The advantages of such combination include the fact that no blind directions are present for circularly polarized signals, as can be seen by quadratically averaging the responses to $\psi = 0$ and $\psi = \pi/4$, with the resulting antenna patterns shown in Figs. 14(a) and 14(b), respectively. The composite detector is blind only to the cross polarization component of the GW propagating in the XY plane ($\theta = \pi/2$) [see Fig. 14(c)].

These features of the antenna pattern are the same of the ordinary single-mass DUAL [13].

B. Optimal tapered configurations

In Sec. III we considered as standard material the Mo, for which the low dissipation factor and the good cross-section to GWs are well characterized [29]. However, there

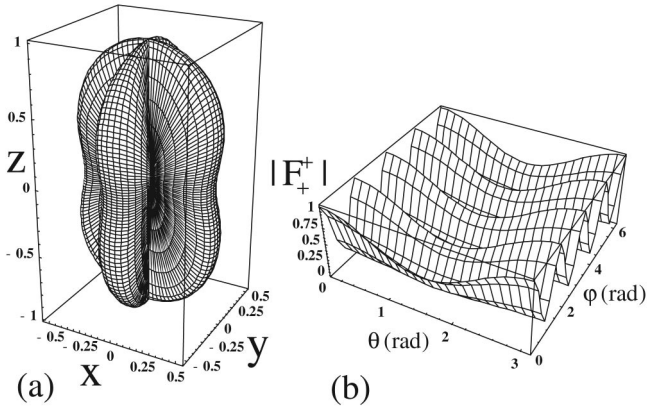

FIG. 12. Detector response function: (a) in Cartesian coordinates and (b) in spherical-polar coordinates, for cylinders equipped with whips [see Figs. 3(b) and 3(c)]. In the panel (a), the distance from a point of the plot surface to the center of the box is just a measure for the GW sensitivity in this direction [see Eqs. (36)]. This plot refers to plus polarized waves.

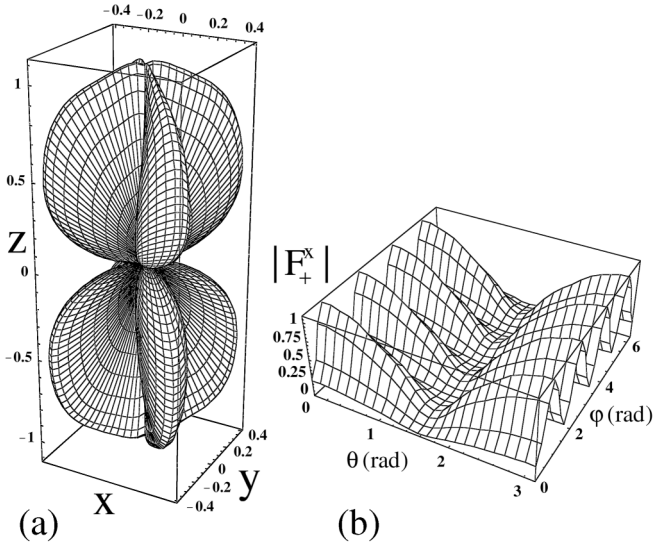

FIG. 13. As in Fig. 12, but for cross polarized GWs.

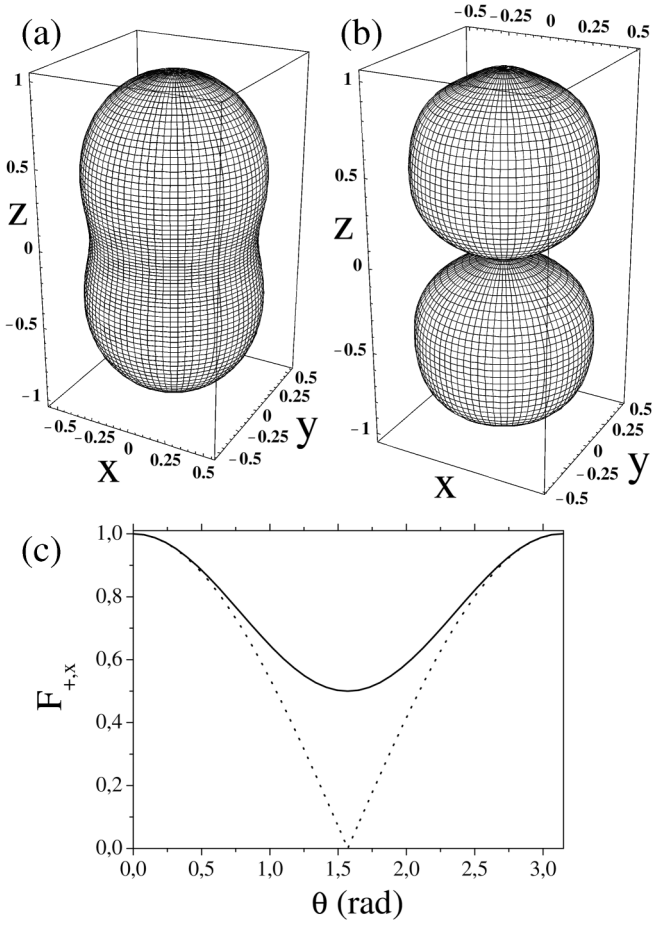

FIG. 14. (a) Antenna pattern $|F^{+}_{+,\times}|$ obtained by quadratically averaging the responses to $\psi = 0$ waves of two tapered detectors, rotated by 45°. (b) Antenna pattern $|F^{\times}_{+,\times}|$ given by the quadratic average of the responses to $\psi = \pi/4$ waves of two tapered detectors, 45° apart. (c) Antenna patterns $|F^{+}_{+,\times}|$ (solid line) and $|F^{\times}_{+,\times}|$ (dotted line) as functions of the θ angle.

are several known materials with a cross-section to GWs considerably higher than that of Mo. Most of them, like for instance diamond, sapphire, or monocrystal SiC, are not a realistic alternative because they cannot be manufactured in large samples using existing technology at reasonable cost. A more realistic choice is C/SiC. This material is a special form of SiC ceramic, that offers design freedom since it can be manufactured in monoblocks of relatively complex shapes [30]. A possible critical issue of C/SiC is its intrinsic dissipation at ultralow temperature, which is currently under investigation. In the following we assume an optimistic value $Q = 10^7$.

The sensitivities for C/SiC tapered cylinders were obtained by scaling (see Sec. II C) the sensitivity curves of the Mo tapered configuration in Fig. 3(c) [31]. We considered 2 detector configurations sensitive in different frequency ranges: a high frequency range [HF $\sim (2 - 5)$ kHz], and a lower frequency range [LF $\sim (1.1 - 2.6)$ kHz]. The HF and LF configurations are targeted to sources such as the NS-NS merger or the BH-BH merger, as discussed in the following section. The resulting spectral sensitivities are shown in Fig. 15 for different operating temperatures. The detector parameters are reported in Table V. The gain in sensitivity of the C/SiC material with respect to Mo is a factor ~1.5 in the strain sensitivity.

As results from Fig. 15, the LF massive configurations produce spectral sensitivities in terms of strain better than those of the HF detectors. However, the mass of these HF detectors is ~4 ton, a figure which would allow us to house many such detectors in small research infrastructures at different locations. Then, a proper joint data analysis from such potentially independent detectors would allow us to obtain a more reliable identification of gravitational signals with respect to a single massive detector.

C. Selected GW sources

Predicted $h(t)$ waveforms have recently become available for some potential sources of GWs in the frequency range of the proposed detectors: in particular, the merger of NS binaries [33,34] and of BH binaries [35]. For both sources we used the predicted numerical $h(t)$ to compute their SNR for the proposed detector configurations, assuming a source distance of 19 Mpc (Virgo cluster) and an incoming direction along the axis of the tapered cylinder.

We report here the optimal SNR, i.e., the one achievable with a Wiener matched filter:

$$\mathrm{SNR} = \sqrt{\frac{2}{\pi}\int_0^{+\infty} \frac{|\tilde{h}(\omega)|^2}{S_{hh}(\omega)}\, d\omega}. \tag{37}$$

The proposed configuration of a pair of identical tapered cylinders, rotated by 45° with respect to each other, allows

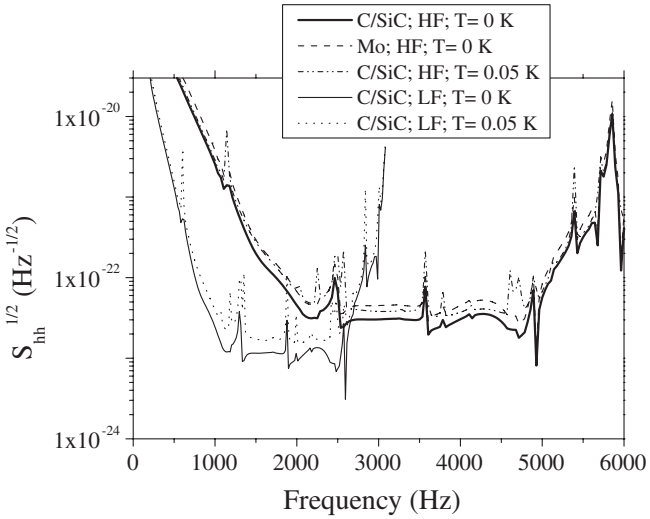

FIG. 15. Comparison among the sensitivity curves of tapered cylinders [see Fig. 3(c)], made of (i) Mo in the higher frequency band (HF), (ii) C/SiC in a HF band, and (iii) C/SiC in a lower band (LF). The effect of thermal noise is also shown.

TABLE V. Geometrical parameters, mass and noise stiffness of tapered Mo and C/SiC cylinders, relative to the sensitivity curves of Fig. 15.

	r_{ext} (m)	r_{int} (m)	L (m)	M (ton)	k_0 (N/m)
Mo; HF	0.35	0.091	1.19	4.4	5.6×10^7
C/SiC; HF	0.54	0.14	1.83	4.1	5.2×10^7
C/SiC; LF	1.02	0.26	3.47	28	1.0×10^8

us to measure both GW polarization components. Therefore, the resulting combined SNR is $(\mathrm{SNR}^2_{h_+} + \mathrm{SNR}^2_{h_\times})^{1/2}$, where $\mathrm{SNR}_{h_{+,\times}}$ represents the SNR calculated by considering only one wave polarization (plus or cross). Since all the considered sources give almost circularly polarized signals, the combined SNR results greater than the $\mathrm{SNR}_{h+,\times}$ by a factor $\sim\sqrt{2}$.

1. Merger of binary NSs

The main scientific interest on such sources relies in the merger and post-merger phases, which carry the information on the equation of state of the NS; therefore, we excluded from our SNR computations the $h(t)$ of the preceding inspiral phase. In the following we consider three models for the NS-NS merger.

According to Ref. [33], a hypermassive NS of ellipsoidal shape can be formed after the merger of two NSs of 1.3 solar masses each (model APR1313 [33]). As a consequence, a long transient of GWs with an approximately constant frequency of about 3.2 kHz is released [33]. The amplitudes for plus and cross polarized GWs, observed at a distance of 100 Mpc from this source, are plotted in Fig. 16, assuming that the angular momentum of the source is aligned with the line of sight.

The resulting SNRs for circularly polarized GWs emitted from the APR1313 model, at an assumed distance of 19 Mpc, are shown in Fig. 17. They refer to the HF C/SiC sensitivity curves of Fig. 15, since the merger frequency of 3.2 kHz is included in the frequency band of this configuration. In order to take into account the merger phase, but not the inspiral, we used the plotted plus and cross components for APR1313 starting from 1.7 ms and 1.8 ms, respectively. According to Ref. [33], since the signal is expected to last for 50 ms, significantly larger than the time window of the available $h(t)$ (see Fig. 16), we included in the reported SNR an improvement of a factor 2 ($\sim 5^{1/2}$) with respect to the shorter waveform plotted in Fig. 16.

We also consider different numerical predictions for the merger of NSs of 1.4 solar masses: A21414 and S1414 [34], with a post-merger signal frequency of ~2.7 kHz and ~1.7 kHz, respectively. The amplitudes for plus and cross polarized GWs, observed at a distance 100 Mpc from the A21414 and S1414 sources, are plotted in Figs. 18 and 19, respectively. According to Ref. [34], the merger phase starts from 7.5 ms and 4.5 ms, respectively, and therefore we considered the following part of their waveforms for our SNR computation. In addition, the authors report that the wave amplitude is underestimated by 40% in the post-merger phase. So, we included this suggested correction in our SNR estimate. The resulting SNRs are plotted in Fig. 20.

For the A21414 source, the SNRs are calculated by considering the HF C/SiC sensitivity curves of Fig. 15, since the post-merger frequency of ~2.7 kHz is included in their frequency band. Similarly, for the S1414 source, the SNRs are estimated by using the LF C/SiC sensitivity curves of Fig. 15, given the post-merger frequency of ~1.7 kHz.

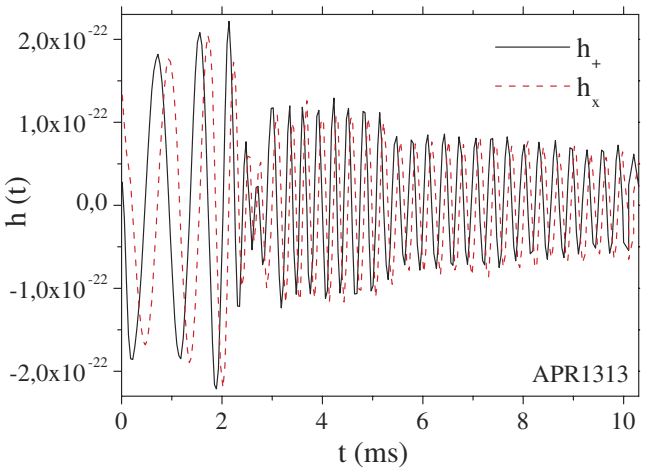

FIG. 16 (color online). Gravitational waveforms plus (h_+, solid line) and cross ($h_\times$, dashed line) for the APR1313 model [33].

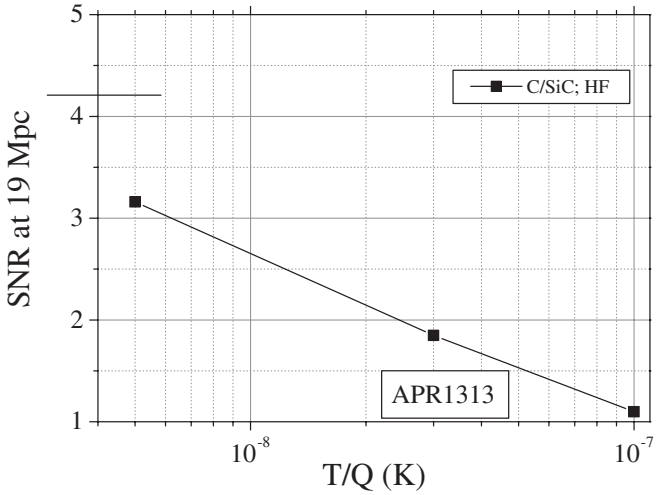

FIG. 17. SNR for circularly polarized GWs emitted by APR1313 source during the merger and post-merger phases, at a distance of 19 Mpc, for the HF C/SiC sensitivities of Fig. 15 versus the thermal noise factor T/Q. The horizontal line, at SNR ~ 4.2, indicates the SNR achievable at the SQL, i.e., neglecting the thermal noise contribution.

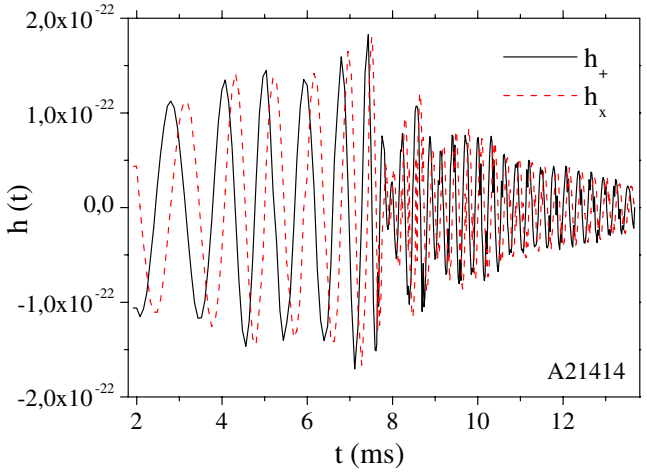

FIG. 18 (color online). Gravitational waveforms plus (h_+, solid line) and cross ($h_\times$, dashed line) for the A21414 model [34].

In summary, a pair of HF C/SiC tapered cylinders, rotated by 45° ($M = 4.1$ ton each, $T/Q \sim 5 \times 10^{-9}$ K, dashed-dotted-dotted curve in Fig. 15), gives SNR ~ 3.2 and ~ 1.7 for the APR1313 and A21414 sources, respectively, at distance of 19 Mpc. Two LF C/SiC tapered cylinders at 45° ($M \sim 28$ ton each, $T/Q \sim 5 \times 10^{-9}$ K, dotted curve in Fig. 15), give SNR ~ 3.5 for the S1414 source at 19 Mpc. These figures are comparable to those computed for Advanced LIGO in Refs. [33,34]. To reach SNR ~ 6 [36] we would need 4, 12, and 3 pairs of such tapered detectors for the APR1313, A21414, and S1414 sources, respectively.

2. Merger of binary BHs

The GWs emitted by a merger of binary equal mass BHs are described in Ref. [35] (see Fig. 21). By scaling these

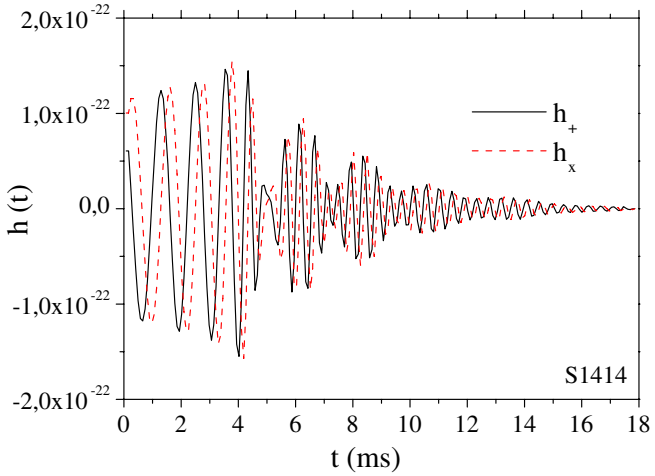

FIG. 19 (color online). Gravitational waveforms plus (h_+, solid line) and cross ($h_\times$, dashed line) for the S1414 model [34].

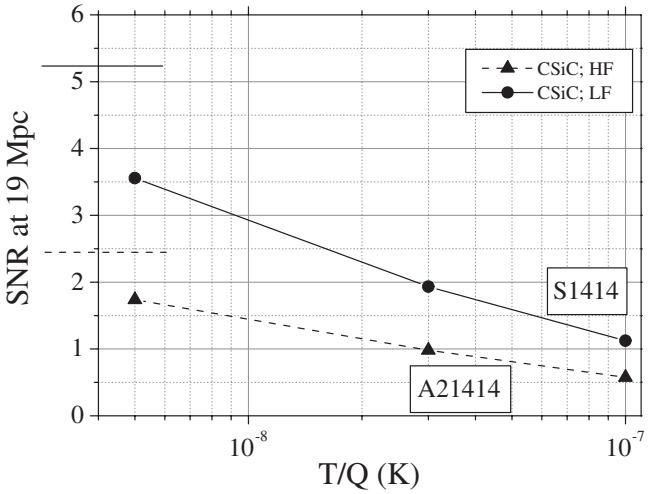

FIG. 20. The solid line refers to the SNRs for circularly polarized GWs emitted by S1414 source at a distance of 19 Mpc, for the LF C/SiC sensitivity curves of Fig. 15 versus the thermal noise factor T/Q; the corresponding horizontal solid line, at about 5.2, indicates the SNR obtained neglecting the thermal noise contribution. The dashed line represents the SNRs for circularly polarized GWs emitted by A21414 source at a distance of 19 Mpc, for the HF C/SiC sensitivity curves of Fig. 15 versus the thermal noise factor T/Q; the corresponding horizontal dashed line, at ~ 2.4, indicates the SNR obtained without considering the thermal noise contribution. All SNRs are computed taking into account only the merger and post-merger phases.

waveforms at the distance of 19 Mpc, we obtain a graph of the SNR for configurations of tapered C/SiC cylinders versus the two BHs total mass (see Fig. 22).

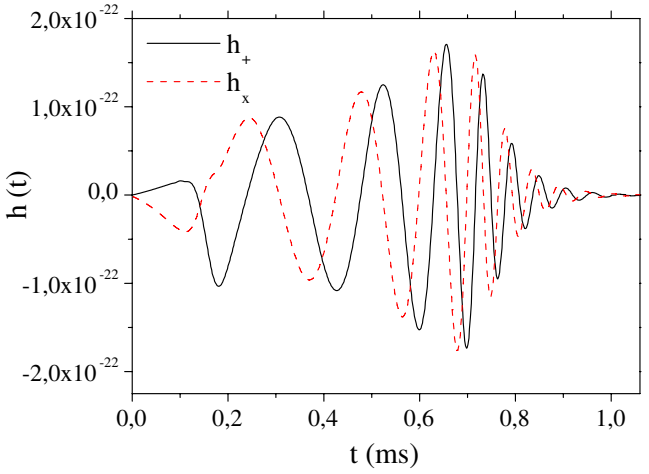

FIG. 21 (color online). Gravitational waveforms plus (h_+, solid line) and cross ($h_\times$, dashed line) for the merger of two BHs at a distance of 100 Mpc: each BH has a mass of 0.5 solar masses [35]. The waveforms can be considered reliable starting from 0.3 ms and consist of the chirp, merger, and ringdown phases.

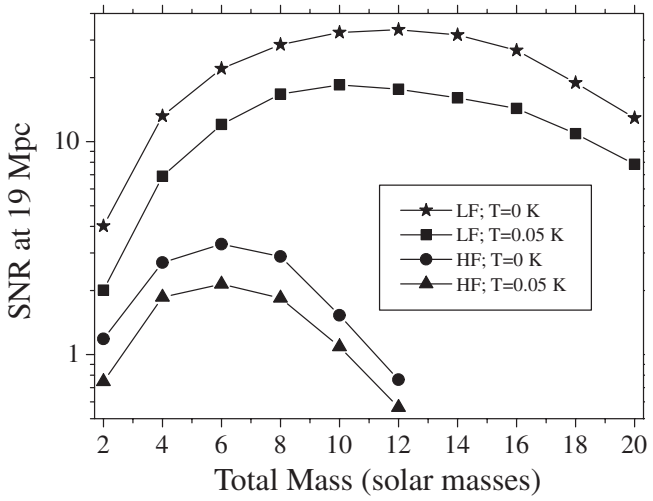

FIG. 22. SNR at 19 Mpc for pairs of the C/SiC detectors (Fig. 15, $Q = 10^7$) versus the total mass of a two BHs system.

For two merging BHs of total mass 12 solar masses, we obtain SNR $\simeq$ 33.5 for the LF C/SiC detector at SQL (solid curve in Fig. 15). When a temperature of 0.05 K is considered, the best SNR is equal to 18.5 for two merging BHs of total mass 10 solar masses. These values refer to pairs of detectors, rotated by $\pi/4$ with respect to each other, $M =$ 28 ton each. For the HF C/SiC detectors of $M = 4.1$ ton, the highest SNR is 3.3 for binary BHs of total mass 6 solar masses, neglecting the thermal noise contribution. When a thermal noise factor $T/Q \sim 5 \times 10^{-9}$ K is considered, the SNR decreases to 2.1 for the same BH mass. Then, in order to reach for this last case a SNR $\sim$ 6, we need 8 couples of such detectors.

V. CONCLUSIONS

The new design of the GW detectors described here solves the problem of the noise mismatch between test mass and readout while keeping the wideband spectral performances of the previous designs of single-mass DUAL detectors of similar mass and material [13]. The tapering of the test mass makes possible to exploit 5 resonant modes at suitably spaced frequencies, all contributing to the GW cross-section. Moreover, the whips amplify the transverse displacement of the tapered detector quadrupolar modes at the sensing surfaces by a factor 15–30 with respect to the single-mass DUAL model. This allows us to achieve the noise matching with a capacitive transducer with realistic values of bias field and capacitance, $\sim 1 \times 10^8$ V/m and 5×10^{-9} F, respectively. For the first time the model of a wideband acoustic detector has been completed by including a transducer system.

The dynamics of the detectors was simulated on the basis of three-dimensional FEM numerical analyses, by computing the transfer functions to GW and back-action force. In particular, we demonstrated that the SQL sensitivity is not degraded by the decrease in noise stiffness, in fact it is very close to the SQL curve obtained for the ordinary single-mass DUAL configuration, having same dimensions and material.

In this work we also described how the configuration of the detector can be optimized as a function of the target bandwidth of sensitivity. In particular, we considered two case studies of tapered detectors: one operating in the $\sim(1.1 - 2.6)$ kHz band and the other in $\sim(2 - 5)$ kHz band (see Fig. 15). For these configurations, the SQL sensitivity level is at $\sim 1.2 \times 10^{-23}$ Hz$^{-1/2}$ and $\sim 3 \times 10^{-23}$ Hz$^{-1/2}$, respectively.

We pointed out the advantages of considering a composite configuration made by twin detectors with parallel axis but rotated by 45°: in fact such a configuration does not have blind directions. We also presented selected science cases for GW sources at the distance of the Virgo cluster: NSs and BHs mergers. Above 2 kHz, the predicted performances of such twin configurations are comparable to those of advanced interferometers. A further opportunity is to consider a small network of such detectors, so to increase the reach, to improve the reliability of the observatory and help the rejection of local disturbances. This should be easier for the target band at higher frequency, since each detector has smaller mass ($\sim$ 4 ton). However, both for the proposed detectors and advanced interferometers, the expected detection rate is still very low. The NS-NS mergers are expected to occur $\sim$0.02 yr^{-1} within the Virgo cluster range [34] and the predictions for BH-BH mergers are even more rare than the binary NS events [37]. Additional sources of GWs in the frequency band above 1 kHz include quasinormal modes in newly born NSs [38]. Despite the low detection rate, the interest on high frequency GWs is very high since they are a clue to the equation of state of matter at extreme densities.

Experimental investigations are in progress to demonstrate the feasibility on small scale prototypes and to characterize the mechanical dissipations of construction materials at low temperatures.

ACKNOWLEDGMENTS

We are grateful to Massimo Cerdonio for fruitful and stimulating discussions. This work was supported by European Community (project ILIAS, Contract No. RII3-CT-2004-506222), Provincia Autonoma di Trento (project QL-Readout), European Gravitational Observatory (R&D grant ''Wideband transducer for DUAL detector'').

APPENDIX A: EQUIVALENT FORCE AND DISPLACEMENT NOISE OF A CAPACITIVE TRANSDUCER COUPLED TO A SQUID AMPLIFIER

Let us consider a generic elastic test mass, whose deformation is sensed by a readout composed of a capacitive transducer followed by a dc SQUID as current amplifier.

The deformation of the test mass is described by the observable X, according to Eq. (1). The back-action response of the test mass, as seen from the sensing port, is described by the transfer function $T_{\mathrm{BA}}(\omega)$ or by its inverse, the dynamical stiffness $k(\omega)$. In general, any linear displacement sensor, based on some kind of intermediate transducer, can be replaced by an equivalent displacement amplifier, characterized by an additive displacement noise source, x_n, and a force noise source, f_n. In addition, the transducer modifies the effective response of the test mass to an external force. In this section we derive an explicit expression of $\tilde{x}_n$, $\tilde{f}_n$ and of the modified stiffness $k'(\omega)$, for the case of a capacitive transducer with a SQUID amplifier.

The circuit that we wish to analyze is shown in Fig. 23. As we are interested in determining the general properties of the capacitive-SQUID readout, we characterize the test mass with a generic dynamic stiffness $k(\omega)$, without any other specification. Then, we rewrite the equation of motion of the electromechanical system in the frequency domain, without projecting on to the normal modes as in Sec. II D:

$$\begin{pmatrix} k(\omega) & -E_0 & 0 & 0 \\ -E_0 & -\omega^2 L_p + i\omega R + 1/C & -\omega^2 M_{tr} & 0 \\ 0 & -\omega^2 M_{\mathrm{tr}} & -\omega^2 L_t & 0 \\ 0 & 0 & -i\omega & 1 \end{pmatrix} \cdot \begin{pmatrix} \tilde{X} \\ \tilde{Q} \\ \tilde{Q}_s \\ \tilde{I} \end{pmatrix} = \begin{pmatrix} \tilde{F}_e \\ \tilde{V}_{\mathrm{th}} \\ \tilde{V}_n \\ \tilde{I}_n \end{pmatrix}. \tag{A1}$$

Here, the first equation in the system (A1) comes directly from Eq. (27). Since we are only interested in finding the properties of the readout, we include in the term $\tilde{F}_e$ all external or internal forces acting on the test mass other than the transducer back-action. The other three equations in the system (A1) are directly derived from Eqs. (32).

Solving the system of linear Eqs. (A1) for the displacement $\tilde{X}$, we obtain

$$\tilde{X} = \frac{1}{k'}(\tilde{F}_e + \tilde{f}_n), \tag{A2}$$

where we defined the modified stiffness $k'(\omega)$ as

$$k'(\omega) = k(\omega) - \frac{E_0^2}{-\omega^2 L_r + i\omega R + 1/C}, \tag{A3}$$

the equivalent force noise

$$\tilde{f}_n = \alpha\left(\frac{\tilde{V}_n}{i\omega} - \frac{L_t}{M_{tr}}\frac{\tilde{V}_{\mathrm{th}}}{i\omega}\right), \tag{A4}$$

and the parameter $\alpha(\omega)$ as

$$\alpha(\omega) = \frac{-i\omega E_0 M_{\mathrm{tr}}/L_t}{-\omega^2 L_r + i\omega R + 1/C}. \tag{A5}$$

Solving Eqs. (A1) for the measured current $\tilde{I}$, we find

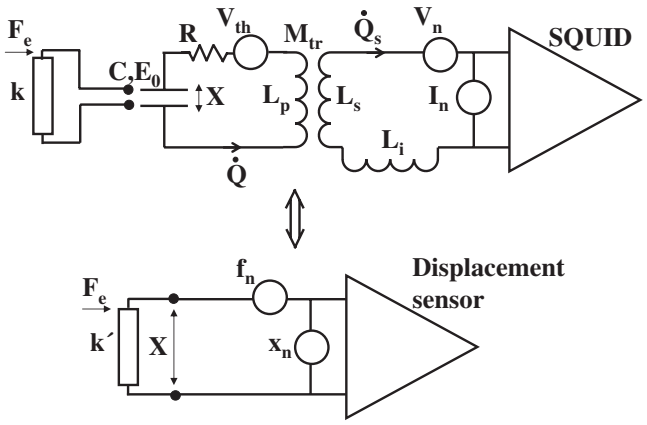

FIG. 23. Scheme of a displacement sensor based on a capacitive transducer and a SQUID amplifier, and equivalent circuit. The noise sources of the equivalent displacement sensor, the additive displacement noise, x_n, and back-action force noise f_n, are functions of I_n,V_n, and V_{th}. The presence of the transducer has the further important effect of loading the test mass to be measured, modifying its dynamical stiffness k into k'. For details on the other parameters see Fig. 1.

$$\tilde{I} = \alpha(\tilde{X} + \tilde{x}_n), \tag{A6}$$

where the equivalent displacement noise $\tilde{x}_n$ is defined by

$$\tilde{x}_n = \frac{1}{\alpha}\left(I_n + \frac{V_n}{i\omega L_t}\frac{-\omega^2 L_p + i\omega R + 1/C}{-\omega^2 L_r + i\omega R + 1/C} - \frac{i\omega V_{\mathrm{th}} M_{\mathrm{tr}}/L_t}{-\omega^2 L_r + i\omega R + 1/C}\right). \tag{A7}$$

It is straightforward to verify that Eqs. (A2)–(A6) define the sources x_n and f_n, and the modified stiffness k' consistently with the equivalent circuit shown in Fig. 23. Moreover, we can interpret α as a transducer efficiency, as it represents the ratio of the measured current $\tilde{I}$ to the effective displacement $\tilde{X}$. We discuss briefly the details of the expressions of α, k', $\tilde{f}_n$, and $\tilde{x}_n$. As regards k', we observe that the presence of the transducer loads the test mass with an additional stiffness, that becomes huge at the unloaded electrical resonance $\omega_{\mathrm{el}} = (L_r C)^{-1/2}$, together with the transducer efficiency α. In other words, for $\omega \simeq \omega_{\mathrm{el}}$ the coupling between the test mass and the SQUID becomes very large, but at the same time the transducer "freezes" the motion of the test mass. As regards the force noise $\tilde{f}_n$, it is composed of a term proportional to the SQUID voltage noise $\tilde{V}_n$, and a term proportional to the electric thermal noise $\tilde{V}_{\mathrm{th}}$. Finally, the displacement additive noise $\tilde{x}_n$, besides a term coming from the SQUID additive noise, features also two terms deriving from the current induced in the electrical circuit by the SQUID voltage noise $\tilde{V}_n$ and by electrical thermal noise $\tilde{V}_{\mathrm{th}}$. These terms introduce an unavoidable correlation between

the displacement and force noise, even if the amplifier noise sources were uncorrelated.

The exact expression of the power spectral density of force and displacement noise, as well their cross-correlation, can be computed by using Eqs. (A4) and (A7). It is possible to show that, under reasonable assumptions, the noise stiffness k_R, defined by Eq. (9), is of the order of $E_0^2 C$ over a given bandwidth around the electrical resonance frequency. For instance, let us assume an idealized mechanical system with constant mechanical stiffness k, and the specific set of transducer parameters listed in Table IV. For the determination of the effective noise stiffness of the readout, one must take into account the transducer loading on the test mass. Therefore, the noise matching condition [see Eq. (10)] must be slightly modified by replacing k with k', as given by Eq. (A3). The ratio $|k_R/k'|$ is then numerically calculated for a transducer with bias field such that $E_0^2 C = k$ (Fig. 24). It is found that the ratio is of the order of 1 over a 2 kHz bandwidth around the electrical resonance frequency, meaning that the noise matching condition $|k_R| \approx |k'|$ is achieved. Therefore, the transducer is matched to the mechanical system when the quantity $E_0^2 C$ is equal to the unloaded stiffness k. In other words, the transducer behaves roughly as if it had an effective noise stiffness of the order of $E_0^2 C$ without loading the test mass.

APPENDIX B: OPTIMIZATION OF TAPERED CYLINDER LENGTH

In this appendix we discuss the choice of the length of the cylindrical detectors proposed in Sec. III. The relevant issue is that the form factor, i.e., the ratio between the cylinder length L and the external radius r_{ext}, can significantly affect the shape of sensitivity curve. In general, this is not true in the plain strain approximation, in which only modes independent of L are considered.

Figure 25 shows the strain sensitivities of the cylindrical detectors proposed in Sec. III, evaluated by means of FEM simulations in plain strain approximation. We note these sensitivity curves are consistent with the three-dimensional curves plotted in Fig. 5. The only relevant difference is the presence of some additional narrow peaks in the three-dimensional curves. These peaks are actually related with spurious modes, not sensitive to GWs, which are not perfectly filtered out by the selective readout.

In general, the frequency and the coupling to the readout of the spurious modes depend strongly on the form factor of the test mass. In particular, the density of spurious modes tends to increase with the increasing length. Thus, we have to find a trade-off between high sensitivity (high length) and a reasonably wide, flat and clean sensitivity band (low length).

The SQL sensitivities for the new configurations of Figs. 3(b) and 3(c) are shown in Figs. 26 and 27, together with the $H_{\mathrm{GW}}(\omega)$ and $T_{\mathrm{BA}}(\omega)$ transfer functions, for a few selected detector lengths. For the configuration in Fig. 3(b), the best trade-off between a flat bandwidth and a good level of sensitivity is achieved for $L = 1.7$ m. For $L = 1.2$ m the sensitivity level is not better, and for $L = 1.9$ m an annoying spurious peak appears in the middle of the sensitive band. For the tapered cylinder in Fig. 3(c), the best trade-off is achieved for $L = 1.19$ m. For $L = 1.47$ m, the density of spurious peaks is quite larger, and for $L = 0.84$ m there is no significant improvement.

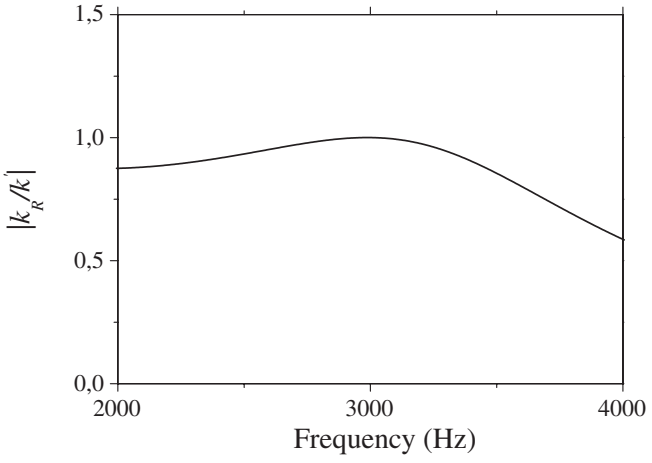

FIG. 24. Ratio $|k_R/k'|$ for the following case: constant unloaded mechanical stiffness k, experimental transducer parameters listed in Table IV, $\nu_{\mathrm{el}} = 3$ kHz, and E_0 chosen so that $E_0^2 C = k$. The ratio $|k_R/k'|$ is of the order of 1 over a 2 kHz bandwidth around ν_{el}, meaning that the noise matching condition is achieved. This shows that the transducer behaves roughly as if it had a noise stiffness of the order of $E_0^2 C$ without loading the test mass.

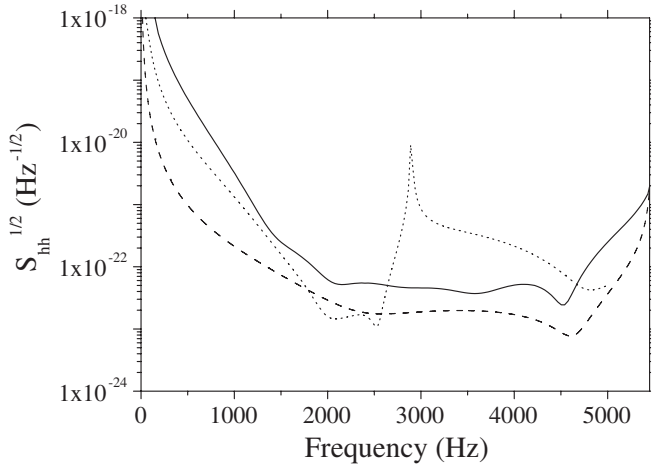

FIG. 25. Comparison among the plain strain SQL sensitivities for the cylinders in Fig. 3(a) (dashed curve), Fig. 3(b) (dotted curve), and Fig. 3(c) (solid curve).

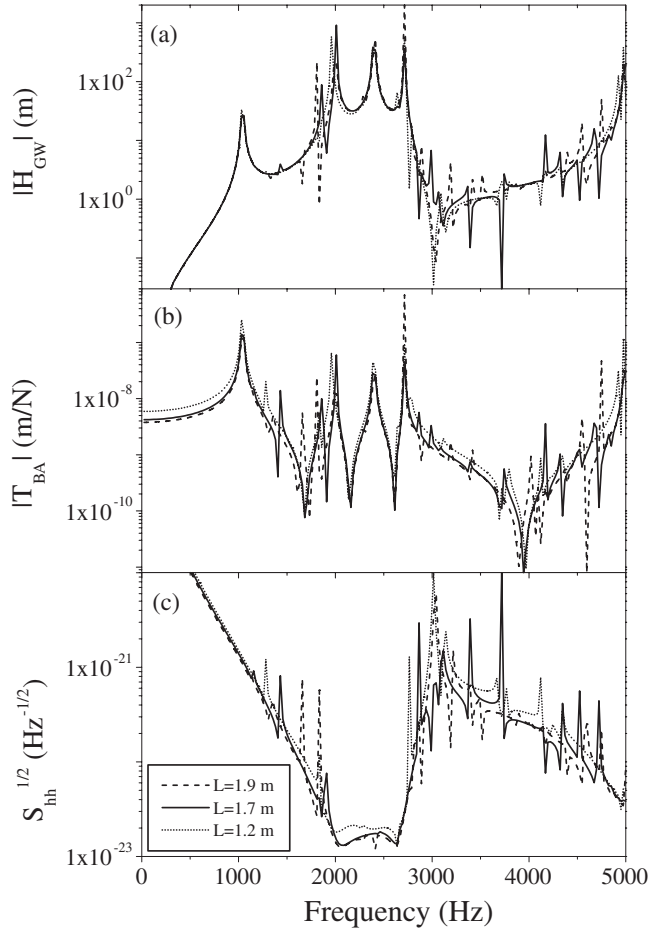

FIG. 26. (a) GW transfer function $|H_{\mathrm{GW}}(\omega)|$, (b) back-action transfer function $|T_{\mathrm{BA}}(\omega)|$, and (c) SQL sensitivities for a cylinder equipped with whips as the one in Fig. 3(b), with $r_{\mathrm{ext}} = 0.5$ m, $r_{\mathrm{int}} = 0.08$ m, but for different lengths L. The detector mechanical stiffness and the sensitivity obtained with unity SNR are: (i) $k_0 = 5.3 \times 10^8$ N/m and $\tilde{H} = 2.5 \times 10^{-25}$ Hz^{-1} for the dashed curve, (ii) $k_0 = 5 \times 10^8$ N/m and $\tilde{H} = 2.7 \times 10^{-25}$ Hz^{-1} for the solid curve, (iii) $k_0 = 3 \times 10^8$ N/m and $\tilde{H} = 2.8 \times 10^{-25}$ Hz^{-1} for the dotted curve.

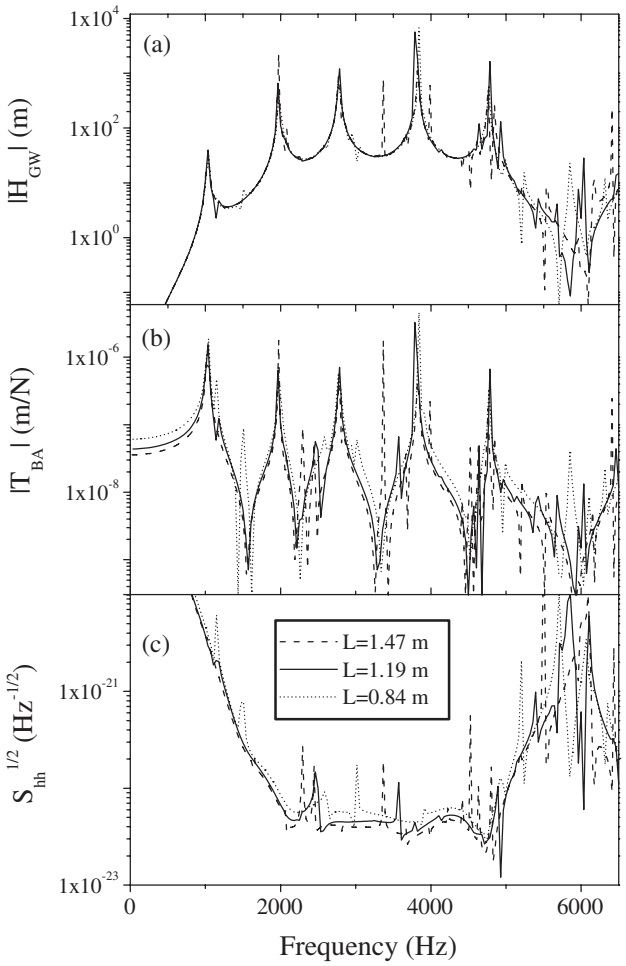

FIG. 27. (a) GW transfer function $|H_{\mathrm{GW}}(\omega)|$, (b) back-action transfer function $|T_{\mathrm{BA}}(\omega)|$, and (c) SQL sensitivities for a tapered cylinder as the one in Fig. 3(c), with $r_{\mathrm{ext}} = 0.35$ m, $r_{\mathrm{int}} = 0.091$ m, but for different lengths L; $k_0 = 7 \times 10^7$ N/m and $\tilde{H} = 3.4 \times 10^{-25}$ Hz^{-1} for the dashed curve, $k_0 = 5.6 \times 10^7$ N/m and $\tilde{H} = 3.6 \times 10^{-25}$ Hz^{-1} for the solid curve, $k_0 = 4.2 \times 10^7$ N/m and $\tilde{H} = 4.6 \times 10^{-25}$ Hz^{-1} for the dotted one.

[1] LIGO, http://www.ligo.caltech.edu.
[2] VIRGO, http://www.virgo.infn.it.
[3] B. Abbott *et al.*, Classical Quantum Gravity **24**, 5343 (2007).
[4] B. Abbott *et al.*, arXiv:0704.3368 [Phys. Rev. D (to be published)].
[5] P. Astone *et al.*, Phys. Rev. D **68**, 022001 (2003).
[6] P. Astone *et al.*, Phys. Rev. D **76**, 102001 (2007).
[7] H. J. Paik, in *Experimental Gravitation*, edited by B. Bertotti (Academic, New York, 1974), p. 515.
[8] J.-P. Richard, Phys. Rev. Lett. **52**, 165 (1984).
[9] L. Baggio *et al.*, Phys. Rev. Lett. **94**, 241101 (2005).
[10] L. Gottardi, Phys. Rev. D **75**, 022002 (2007).
[11] M. Cerdonio, L. Conti, J. A. Lobo, A. Ortolan, L. Taffarello, and J. P. Zendri, Phys. Rev. Lett. **87**, 031101 (2001).
[12] M. Bonaldi, M. Cerdonio, L. Conti, M. Pinard, G. A. Prodi, L. Taffarello, and J. P. Zendri, Phys. Rev. D **68**, 102004 (2003).
[13] M. Bonaldi, M. Cerdonio, L. Conti, P. Falferi, P. Leaci, S. Odorizzi, G. A. Prodi, M. Saraceni, E. Serra, and J. P. Zendri, Phys. Rev. D **74**, 022003 (2006).
[14] F. N. H. Robinson, *Noise and Fluctuations in Electronic Devices and Circuits* (Clarendon Press, Oxford, 1974).
[15] D. G. Blair, A. Giles, and M. Zeng, J. Phys. D **20**, 162 (1987).
[16] P. Saulson, *Fundamentals of Interferometric Gravitational Wave Detectors* (World Scientific, Singapore, 1994).
[17] H. B. Callen and T. A. Welton, Phys. Rev. **83**, 34 (1951).
[18] S. Kobayashi, IEEE Trans. Dielectr. Electr. Insul. **4**, 841

(1997).
[19] V. B. Braginsky and F. Y. Khalili, *Quantum Measurement* (Cambridge University Press, Cambridge, 1992).
[20] M. Bonaldi, M. Saraceni, and E. Serra, J. Mech. Des. **130**, 042302 (2008).
[21] M. Bonaldi (private communication).
[22] R. J. Duffin, SIAM J. Appl. Math. **17**, 179 (1969).
[23] L. Meirovitch, *Principles and Techniques of vibrations* (Prentice-Hall, London, 1996).
[24] P. Rapagnani, Nuovo Cimento Soc. Ital. Fis. C **5**, 385 (1982).
[25] P. Falferi, M. Bonaldi, M. Cerdonio, A. Vinante, R. Mezzena, G. A. Prodi, and S. Vitale, Appl. Phys. Lett. **88**, 062505 (2006).
[26] A. Vinante, Classical Quantum Gravity **23**, S103 (2006).
[27] A. Marin *et al.*, Classical Quantum Gravity **19**, 1991 (2002).
[28] ANSYS, Inc., Southpointe, 275 Technology Drive, Canonsburg, PA 15317, http://www.ansys.com.
[29] W. Duffy, Jr., J. Appl. Phys. **72**, 5628 (1992).
[30] B. Harnisch, B. Kunkel, M. Deyerler, S. Bauereisen, and U. Papenburg, ESA Bull. **95**, 107 (1998).
[31] In order to check the validity of the scaling formulas in the case of different Poisson's ratios, we performed three-dimensional FEM simulations of two tapered detectors of identical dimensions and material, but with different Poisson's ratios, of 0.31 and 0.17 [32], corresponding to the Mo and C/SiC materials, respectively. The discrepancy between the resulting sensitivity curves appears almost negligible. This suggests that the scaling formulas are approximately valid also in the case of materials with significantly different Poisson's ratio.
[32] Cesic by ECM, http://www.cesic.de.
[33] M. Shibata and K. Taniguchi, Phys. Rev. D **73**, 064027 (2006).
[34] R. Oechslin and H.-T. Janka, Phys. Rev. Lett. **99**, 121102 (2007).
[35] M. Campanelli, C. O. Lousto, and Y. Zlochower, Phys. Rev. D **73**, 061501(R) (2006).
[36] From the previous experiences of the network of bar detectors [5,6], the SNR thresholds used to search candidate GW signals with high confidence can be slightly lower than SNR $= 6$. The same would hold for any network of detectors showing pure Gaussian noise statistics. In practice however, it is extremely difficult to give a realistic estimate of the detection threshold of future detector networks, since the balance between false alarm rates and false dismissal probability can be determined only keeping into account a realistic statistics of the noise excesses from the Gaussian model. This task is well beyond the scope of this paper and therefore we will keep SNR ~ 6 as an indication of what is likely to be detectable with high confidence by a network of tapered cylinders.
[37] K. Belczynski, R. E. Taam, V. Kalogera, F. A. Rasio, and T. Bulik, Astrophys. J. **662**, 504 (2007).
[38] V. Ferrari, G. Miniutti, and J. A. Pons, Mon. Not. R. Astron. Soc. **342**, 629 (2003).